A binary-tree based model for rate-independent polycrystals

Sivasambu Mahesh [a]

[a] *Departments of Mechanical and Aerospace Engineering, Indian Institute of Technology, Kanpur 208016. India.*

Abstract

A model of a rigid-plastic rate-independent polycrystalline aggregate wherein sub-aggregates are represented as the nodes of a binary tree is proposed. The lowest nodes of the binary tree represent grains. Higher binary tree nodes represent increasingly larger sub-aggregates of grains, culminating with the root of the tree, which represents the entire polycrystalline aggregate. Planar interfaces are assumed to separate the sub-aggregates represented by the binary tree. Equivalence between the governing equations of the model and a standard linear program is established. The objective function of the linear program is given by the plastic power associated with polycrystal deformation and the linear constraints are given by compatibility requirements between the sub-aggregates represented by sibling nodes in the binary tree. The deviatoric part of the Cauchy stresses in the sub-aggregates are deduced as linear combinations of the Lagrange multipliers associated with the constraints. It is shown that the present model allows a generalization of Taylor's principle to polycrystals. The proposed model is applied to simulate tensile, compressive, torsional, and plane-strain deformation of copper polycrystals. The predicted macroscopic response is in good agreement with published experimental data. The effect of the initial distribution of the planar interfaces separating the sub-aggregates represented by the binary tree on the predicted mechanical response in tension, compression and torsion is studied. Also, the role of constraints relaxation in simulations of plane strain compression is investigated in detail.

Key words: Crystal plasticity, Binary tree, Texture modeling, Numerical Algorithms

1 Introduction

1.1 Models of polycrystal plasticity

Over the past two decades intense effort has been directed toward developing the capability to numerically simulate the plastic response of realistic bodies subjected to complex macroscopic deformation processes while accounting for microstructural evolution using detailed models (Mathur and Dawson, 1989, Beaudoin et al., 1993, 1995, Mika and Dawson, 1998, Barbe et al., 2001, Ganapathysubramanian and Zabaras, 2005, Logé and Chastel, 2006, Van Houtte et al., 2006, Guan et al., 2006, Haddadi et al., 2006, Amirkhizi and Nemat-Nasser, 2007, Barton et al., 2008). A promising strategy to this end, proposed by Dawson and co-workers (Mathur and Dawson, 1989, Beaudoin et al., 1993, 1995, Mika and Dawson, 1998), involves embedding a microscopic polycrystal model within each element of a macroscopic finite element mesh. In this approach the microscopic model supplies the material response to the macroscopic finite element, which in turn determines the deformation imposed upon the microscopic model. Since the computational time spent on the microscopic model takes up much of the simulation time (Barton et al., 2008), novel methodologies to reduce the number of evaluations of the microscopic model have been proposed. Examples of such techniques are those due to Kalidindi and co-workers (Kalidindi and Duvvuru, 2005, Kalidindi et al., 2006, Knezevic et al., 2008) to extract the microscopic response from a database using spectral interpolation, and those based on adaptive sampling developed by Arsenlis et al. (2006), and Barton et al. (2008). Also, in order to reduce the computational effort of evaluating the microscopic model, all the aforementioned simulations represent the polycrystal using the computationally light Taylor (1938) model.

The Taylor model assumes that the deformation experienced by each grain in the polycrystal equals the macroscopic deformation imposed upon the polycrystal. It thus ensures compatibility between grains while ignoring traction continuity and intergranular interactions. Nevertheless, the Taylor model successfully predicts the qualitative evolution of texture in symmetric materials (Hirsch and Lucke, 1988a,b). However, as discussed by Leffers (1975, 1978), Hirsch and Lucke (1988a,b), and Leffers and Christoffersen (1997), the Taylor model suffers from several shortcomings such as its tendency to overestimate texturing rate, its inability to predict the formation of certain experimentally observed texture components, its unsuitability in sub-structural studies, its inability to model intragranular phenomena, its inapplicability to low symmetry materials, etc. Efforts to modify the microstructural model to overcome these shortcomings are significant because predictions of macroscopic simulations sensitively depend on the quality of the microscopic model (Van Houtte

et al., 1999, 2002, 2005).

Successful approaches to modifying the Taylor model invariably hinge upon better approximating the grain level stress in the model (Leffers, 1978, Aernoudt et al., 1993). In perhaps the earliest such approach, Honneff and Mecking (1978) relaxed rolling direction shear constraints in rolling simulations by setting the corresponding shear tractions to zero. They found that this reduced the rate of texturing and led to better comparison between the predicted and experimental textures. The mixed deformation-rate and traction boundary condition of Honneff and Mecking (1978) is known as relaxed constraints. It differs from full constraints wherein all components of the deformation-rate are imposed upon a grain. Relaxed and full constraints are ideally suited when the granular morphology is pan-cake shaped and equiaxed, respectively. Tomé et al. (1984) have provided a technique to effect a transition from full to relaxed constraints with increasing grain aspect ratio.

A second class of models aimed at better approximating the stress-state in the grains are the two-site models wherein the unit of the model polycrystal is a pair of grains instead of a single grain. Such models have been proposed by Lebensohn et al. (1998a), Lebensohn (1999), Van Houtte et al. (1999), Garmestani et al. (2001), Lee et al. (2002), and others. In these models, the macroscopically imposed deformation is accommodated by the deformation of an assembly of two grains. The interface between the grains itself may or may not accommodate part of the imposed deformation. Traction continuity between the grains making up a bicrystal unit is either enforced exactly between pairs of grains as in the LAMEL model of Van Houtte et al. (1999) or approximately as in the ALAMEL model of Van Houtte et al. (2002). An extension of this notion, to assemblies comprised of multiple grains was developed by Engler et al. (2005), and termed the grain interaction model (GIA). GIA considers a group of eight grains on which the macroscopic deformation is imposed. It permits incompatibility between neighboring grains. Excessive incompatibility is however suppressed by penalizing the overall plastic work function by the energy stored in a geometrically necessary dislocation field needed to accommodate the incompatibility (Ashby, 1970).

A third approach using the self-consistent models developed by Kröner (1961), Hill (1965), Molinari et al. (1987), and Lebensohn and Tomé (1993) treats intergranular interactions in an average sense by requiring each grain to deform compatibly with a homogeneous effective medium representing the polycrystal. In this approach the deformation of grains may differ from that of the polcrystal. However, grains need only maintain displacement and traction continuity with a homogeneous effective medium representing the polcrystal. Therefore, intergranular interactions in the self-consistent model are enforced in an average sense with the averaging done over the entire polycrystal. The effect of a grain's neighborhood on its deformation are therefore not captured using this

approach. Self-consistent models embedding two-site models have also been proposed and studied by Lebensohn (1999), Proust et al. (2007), and others.

A fourth approach to calculate the stress and deformation fields associated with the macroscopic deformation of a polycrystal is the crystal plasticity finite element method suggested by Havner (1971), and developed recently by Kalidindi et al. (1992), Beaudoin et al. (1995), and Logé and Chastel (2006). These calculations are capable of accounting for details of the microstructure and intergranular interactions, and avoid assumptions such as the homogeneity of grain deformation that are needed in other models. These models are ideal for studies of intragranular deformation processes as in Zhang et al. (2008), who study necking in an aluminum single crystal, and as in Héripré et al. (2007), who study the intragranular processes in polycrystalline zirconium and titanium alumnide, using this approach. However, these detailed models are prohibitively computationally expensive for embedding within finite elements in calculations. As pointed out by Van Houtte et al. (2002), however, they are useful to verify the assumptions of simpler models that may be amenable to embedding within macroscopic finite-element simulations.

Besides these approaches, a large body of literature exists on phenomenological modeling of the yield surface in a manner consistent with a polycrystal model (Kim et al., 2008, Wang et al., 2008, Van Houtte et al., 2009, and references therein). It suffices for our purposes to note that the potential for a given material developed according to these models will depend on the crystal plasticity model used for parameter identification.

1.2 A binary-tree based model of a polycrystal

In a foregoing article (Mahesh, 2009, henceforth referred to as I), we had proposed a model of a polycrystalline aggregate comprised of rate-dependent grains (Pan and Rice, 1983), wherein we had also introduced a representation of the aggregate by a binary tree. The polycrystal model introduced in I was called the hierarchical model. In order to avoid conflict with the more widespread usage of the term 'hierarchical', we will henceforth refer to the polycrystal model proposed in I as the binary-tree based model. In the binary-tree based model, the polycrystalline aggregate is regarded as comprised of two sub-aggregates, separated by a planar interface across which velocity and traction continuity are enforced. Each of the two sub-aggregates is then subdivided, the sub-aggregates thus formed further subdivided, and so on, until the smallest sub-divisions contain only single grains. To illustrate, Fig. 1 shows the steps involved in constructing a binary-tree based model, and its binary tree representation from a micrograph. In Fig. 1(a), the first division of the polycrystalline aggregate into two sub-aggregates is effected by the nearly vertical

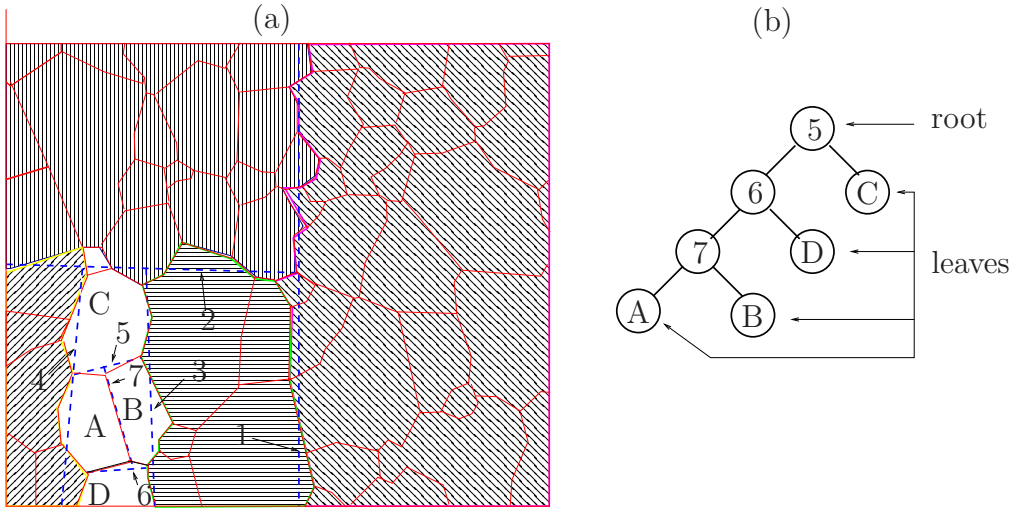

Fig. 1. Construction of a binary tree from a 2D micrograph observed by Manonukul and Dunne (2004). Solid red lines indicate grain boundaries, and dashed blue lines indicate interfaces between sub-aggregates assumed in the binary tree model. (a) The micrograph is divided using the interfaces labeled $1, 2 \ldots, 7$, in that order, to produce sub-aggregates of the polycrystalline aggregate. For clarity, the process of sub-division is shown to completion only in the unhatched part of the micrograph. (b) A representation of the sub-aggregate in the unhatched part of the micrograph formed by grains A, B, C, and D as a binary tree. A general procedure for the recursive generation of a binary tree from a micrograph is given in Mahesh (2009).

interface (dashed line labeled 1). One of the two resulting sub-aggregates, to the right of the dividing vertical line, is shown cross-hatched. Further division only of the other sub-aggregate by interface 2 into upper (vertical hatching) and lower sub-aggregates is shown in Fig. 1a. Although the binary-tree based polycrystal model is constructed by sub-dividing every sub-aggregate formed, for clarity of depiction, the process of subdivision is shown to completion only in a part of the micrograph by introducing interfaces $3, \ldots, 7$, in that order, as shown in Fig. 1(a).

The subdivision of the polycrystal into sub-aggregates, which are contained within each other naturally admits of representation as a binary tree (Cormen et al., 1990). The binary tree representation of the entire polycrystalline aggregate shown in the micrograph of Fig. 1(a) will be very large and is not shown. However, consider the part of the polycrystal comprised of grains A, B, C, and D, shown unhatched in Fig. 1(a). The binary tree corresponding to this aggregate is shown in Fig. 1b. Each node in the binary tree of Fig. 1b represents a sub-aggregate of the aggregate of grains A, B, C, and D. The top most node of this binary tree, labeled its root in Fig. 1b, represents the entire aggregate of grains A, B, C, and D. The lowest nodes of the binary

tree, labeled leaves, represent the grains themselves. Intermediate nodes of the binary tree, that are neither the root nor the leaves of the tree, represent various sub-aggregates. The closer a non-leaf node is to the root, the larger the number of grains in the aggregate it represents. Non-leaf nodes are identified by the interface label separating the two sub-aggregates in Fig. 1b. Thus, node 7 represents a sub-aggregate of grains A and B, node 6 represents a sub-aggregate of grains A, B, and D, and node 5 represents a sub-aggregate of grains A, B, D, and C. The two sub-aggregates constituting a larger granular aggregate in the binary-tree based model are represented in the binary tree as children of the node representing the larger granular aggregate. Thus, the granular aggregate representing node 6 is comprised of the sub-aggregates representing node 7 (grains A and B), and those comprising node D (grain D only). The nomenclature of nodes, root and leaves used here follows standard convention (Cormen et al., 1990). In the sequel, references to nodes of the binary tree and the sub-aggregate represented by them will be used interchangeably. Thus, the 'Cauchy stress in node 7' refers to the Cauchy stress in the sub-aggregate of grains represented by node 7, etc.

The binary tree representation of any four grain sub-aggregate is not the same, but reflects the intergranular interactions determined by the placement of the grains in the microstructure. As examples, Fig. 2 shows two possible binary tree representations of aggregates of four grains, with the representation of Fig. 2b coinciding with that of Fig. 1b. A formal algorithm to determine the structure of the binary tree for a given polycrystalline aggregate was given in I.

The velocity gradient and Cauchy stress in each sub-aggregate (represented by a non-leaf node in the binary tree) is taken as the volume fraction weighted average of the velocity gradients and Cauchy stresses, respectively, in its constituent grains. Thus, the Cauchy stress in the sub-aggregate represented by node 7 in Fig. 1 is taken as the volume-fraction weighted average of the Cauchy stresses in grains A and B, while that in node 6 averages over the stresses in A, B, and D. Also, the interface between the sub-aggregates represented by the children of a node in the binary tree is assumed to be planar, and velocity and traction continuity is enforced between such sub-aggregates. Thus, velocity and traction are required to be continuous across interfaces 7, 6, and 5 in Fig. 1a. This leads to the following interesting consequence for intergranular interactions. Whereas the deformation of grains A and B will be strictly compatible (i.e., occur in a manner that preserves traction and velocity continuity at their common interface, which in this case is a grain boundary), deformation of A and D is also subject to a weaker form of compatibility. This is so, because the deformation of grain D is strictly compatible with node 7, which is nothing but a composite of grains A and B. The velocity and traction fields of node 7 will therefore be determined by those of grain A in part, so that compatibility of nodes 7 and D across their common interface 6 results

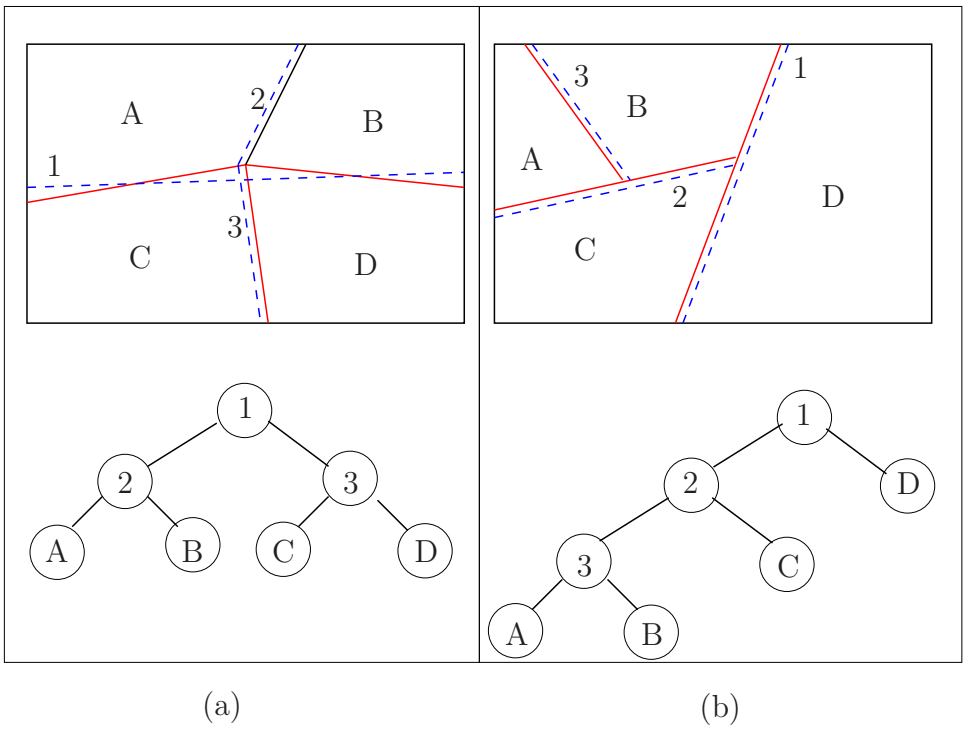

Fig. 2. Schematic drawings of two grain placement schemes for a 4 grain microstructure (first row), and the binary trees corresponding to them (second row). In both cases, node 1 is the root of the tree, and nodes A, B, C, and D are the leaves of the tree denoting grains. The compatibility conditions between the nodes of the tree are however markedly different in case (a) and case (b). The solid and dashed blue lines mean the same as in Fig. 1.

in a weaker form of compatibility between nodes A and D. Thus, although it may appear at first sight that only one intergranular interaction of grain A (with grain B) is considered in the binary-tree based model, grain A interacts with other grains also, by virtue of it forming a part of larger sub-aggregates represented by nodes 7, 6, and 5 in the binary tree of Fig. 1b. Carrying this reasoning further, we see that every grain in the present model interacts with every other grain through compatibility constraints. But the strength of interaction, as measured by the continuity of their velocity and traction fields, varies between different pairs of grains. Thus, the smaller the smallest common sub-aggregate to which two grains belong, the stronger their interaction. The loosely stated notions above will be made precise in Sec. 2.

The binary-tree based model thus overcomes the fundamental shortcomings of both the Taylor (1938) model, wherein intergranular traction continuity is disregarded and the Sachs (1928) model, wherein intergranular velocity continuity is ignored (Gil Sevillano et al., 1980). It also considers the intergranular interactions in greater detail than the self-consistent model, which treats only the interaction of each grain with a homogeneous effective medium representing the polycrystalline aggregate. The binary-tree based model, however,

coarse-grains intergranular interactions, so that unlike a crystal plasticity finite element model (Kalidindi et al., 1992), it is unable to exactly enforce velocity and traction continuity between a grain and its neighbors across multiple grain boundaries simultaneously. However, in modeling the intergranular interactions by coarse graining, the binary-tree based model avoids the huge computational cost of the crystal plasticity finite element approach. Indeed, we found in I that the computational effort required to solve the binary-tree based model and the classical models is of the same order.

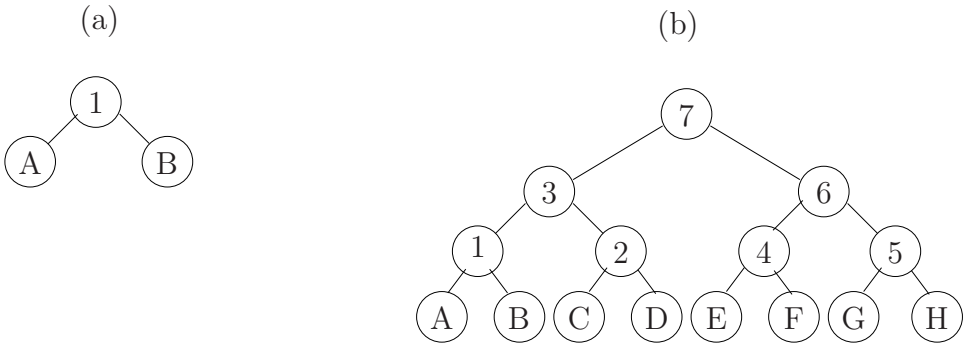

Fig. 3. Binary tree representation of the (a) two-point version of the binary-tree based model used to compare with Lebensohn et al. (1998a), Lebensohn (1999), and Van Houtte et al. (1999), and (b) the eight-point versions of the binary-tree based model used to compare with the GIA model of Engler et al. (2005).

The binary-tree based model also admits of comparison with previously proposed multi-point models following the second approach to polycrystal modeling mentioned in Sec. 1.1. To compare with two-point models, we consider a version of the binary-tree based model wherein the largest aggregates considered are comprised of only two grains, A and ,B represented by the binary tree in Fig. 3a. The polycrystalline response is taken as the average response of such grain pairs. Although the binary-tree based model is more general in that it is not limited to the consideration of two-grain aggregates only, its two-point version coincides with the model of Lebensohn et al. (1998a), Lebensohn (1999), with the Taylor bicrystal model of Lee et al. (2002), and with the LAMEL model of Van Houtte et al. (1999, 2005).

To compare with the eight-point GIA model of Engler et al. (2005), we consider one of several possible representations of an eight grain sub-aggregate in the binary-tree based scheme as shown in Fig. 3b. On the one hand, the GIA model does not enforce strict compatibility of deformation at grain boundaries. The work of deformation is taken to include both the plastic work expended through slip within grains, and the energy stored in the geometrically necessary dislocation walls associated with incompatibilities in the grain boundaries. The minimization of this work of deformation restricts the extent of the

incompatibilities predicted by the GIA model. On other hand, the binary-tree based model enforces compatibility across the common grain boundary of four grain pairs: A and B, C and D, etc., and across the common interfaces between sub-aggregates represented by nodes 1 and 2, 4 and 5, and 3 and 6, for a total of seven compatibility constraints. Thus, the binary-tree based model differs from the GIA model in the treatment of velocity continuity between its constituents. Neither model is contained in the other, as a special case.

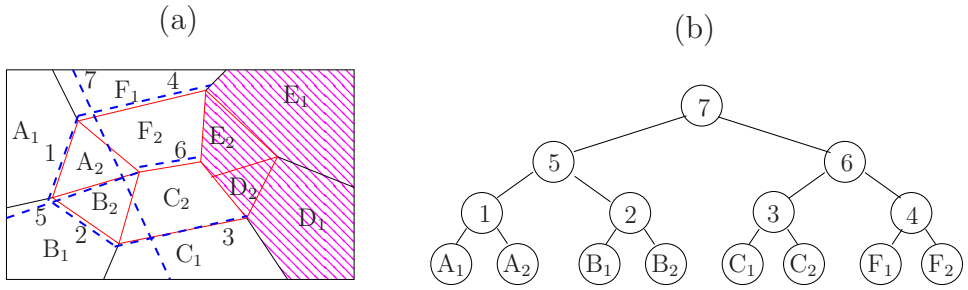

Fig. 4. (a) Discretization of a grain (union of all regions with subscript 2) and its neighbors (regions with subscript 1) according to the ALAMEL model of Van Houtte et al. (2005), and (b) a binary tree representation of a part of its binary-tree based model. Note that (b) corresponds only to the unhatched portion of (a). The solid red and dashed blue lines mean the same as in Fig. 1.

The N-point ALAMEL model of Van Houtte et al. (2005) discretizes the polycrystal into an array of bicrystals, each of which can be treated using the aforementioned LAMEL model. Each bicrystal is formed by 'capturing' a part of the surrounding grains at each grain boundary. Thus, the ALAMEL model replaces the emphasis on uniformity of grain deformation in the Taylor model with an emphasis on compatible deformation across grain boundaries. The binary-tree based model can be regarded as an extension of the ALAMEL model. To construct such a extension, however, a grain with N neighbors must be discretized into N parts, and each part must be regarded as an independent grain. Fig. 4a shows this discretization performed on a schematic grain and its neighborhood. The schematization follows Van Houtte et al. (2005). A division of the schematic microstructure in Fig. 4a by the introduction of interfaces follows the procedure used in Fig. 1 above, and results in the binary tree representation of the binary-tree based model shown in Fig. 4b. The ALAMEL model restricts itself to consideration of the set of two-point binary trees, such as those rooted at nodes 1, 2, 3, and 4 in Fig. 4. The binary-tree based model considers more extensive interactions, thereby justifying our earlier assertion that the binary-tree based model can be regarded as an extension of the ALAMEL model.

The formulation of the binary tree based model given in Sec. 2 begins with formal definitions of quantities associated with the binary tree in Sec. 2.1. After recapitulating the standard kinematics of rigid-plastic rate-independent grains in Secs. 2.2, and 2.3, we extend these notions to arbitrary nodes of the binary tree, i.e., to arbitrary sub-aggregates, in Sec. 2.4. Velocity and traction continuity conditions are then set up in invariant form in Secs. 2.5, and 2.6, and expressed in component form in Sec. 2.8. After these preliminary steps, the key result that the boundary value problem can be reduced to a linear programming problem is given in Sec. 2.9. We then compare the predictions of the present model with the classical models and the rate-dependent binary-tree based models in Sec. 3 and show in Sec. 3.3 that the computational effort of the present model is comparable to that of the classical Taylor model. The comparability of computation time of the present model and the classical Taylor model, and its success in overcoming the shortcomings of the classical Taylor model, make it a model of choice for embedding within macroscopic finite element simulations of complex deformation processes.

2 Model of a rate-independent polycrystal

2.1 Structure of the polycrystal, and the binary tree representation

The structure of the binary-tree based model described in the present work is identical to that in I except that the polycrystal is constituted of rate-independent grains to be described in Sec. 2.2.

Recall from Sec. 1.2 that the binary-tree based model works with sub-aggregates of a polycrystalline aggregate. Its most natural representation is in terms of a binary tree. The lowest nodes of the binary tree are called leaves, and physically represent grains. Higher binary tree nodes represent increasingly larger sub-aggregates of grains, culminating with the root of the tree that represents the entire polycrystalline aggregate. Fig. 5 schematically shows an $N_g = 256$ grain, $2N_g - 1 = 511$ node binary tree that represents the polycrystalline aggregate to be studied in this work. Following standard notation (Cormen et al., 1990), the children of a node k are the two nodes beneath node k, and are denoted $l(k)$ and $r(k)$. Physically, since node k denotes a sub-aggregate of grains, $l(k)$ and $r(k)$ denote smaller sub-aggregates that partition the sub-aggregate denoted by node k. The parent of a node k, is denoted $p(k)$. Note that $p[l(k)] = p[r(k)] = k$ and physically $p(k)$ represents the larger sub-aggregate formed by the union of the sub-aggregates represented by $l(k)$, and

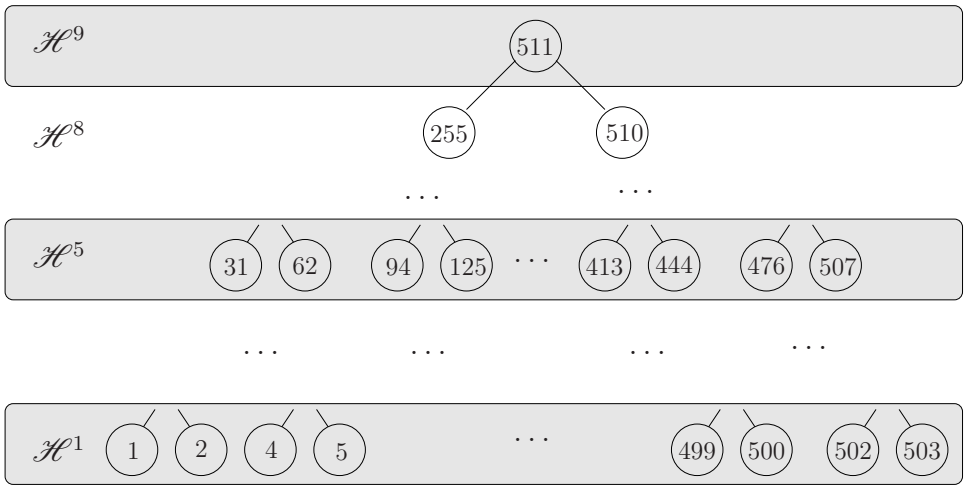

Fig. 5. Balanced binary tree representation of a $2N_g - 1 = 2^h - 1 = 511$ node model of height $h = 9$ modeling a polycrystal of $N_g = 2^{h-1} = 256$ grains. Nodes at the lowest level of the binary tree $(1, 2, \ldots, 502, 503)$, labeled $\mathscr{H}^1$, represent grains. The root of the binary tree, node 511, represents the entire polycrystalline aggregate. Intermediate nodes of the binary tree represent sub-aggregates. Unlike in previous figures, where we designated grains by alphabetical characters, we will use numerals for all the nodes of the binary tree henceforth.

$r(k)$. Two nodes are called siblings if they share a common parent and the sibling relationship is denoted by $s[l(k)] = r(k)$ and $s[r(k)] = l(k)$. Velocity and traction continuity conditions will apply between siblings in the binary tree representation of the model. The root of the binary tree (the topmost node without a parent) is denoted by r, and represents the entire polycrystalline aggregate. In Fig. 5, $r = 511$. The set of all descendants of any node k is denoted $\mathscr{D}[k]$ and is defined as

$$\mathscr{D}[k] = \begin{cases} \{k\}, & \text{if } l(k) \text{ and } r(k) \text{ do not exist,} \\ \{k, \mathscr{D}[l(k)], \mathscr{D}[r(k)]\}, & \text{otherwise.} \end{cases} \tag{1}$$

The above definition has the form of a recurrence, in that it defines $\mathscr{D}[k]$ in terms of the same property of the children of node k, if any. This is a common feature of many properties associated with binary trees.

The subset of $\mathscr{D}[k]$ that are also leaves is denoted $\mathscr{L}[k]$. We also define $\mathscr{N}[k] = \mathscr{D}[k] - \mathscr{L}[k]$, which consists of the descendants of node k that are not leaves. Physically, $\mathscr{D}[k]$ represents all the sub-aggregates of the binary-tree based model contained in the sub-aggregate represented by node k, $\mathscr{L}[k]$ is the set of all the grains in the sub-aggregate represented by node k, and $\mathscr{N}[k]$ is the set of all those sub-aggregates that appear in the binary-tree based model that are subsets of the sub-aggregate represented by node k, but are not grains.

The ancestors of a node k are defined as

$$\mathscr{A}[k] = \begin{cases} \{k\}, & \text{if } p(k) \text{ is undefined,} \\ \{k, \mathscr{A}[p(k)], & \text{otherwise,} \end{cases} \tag{2}$$

and physically represent set of all sub-aggregates in the binary-tree based model in which the sub-aggregate denoted by node k in the binary tree belongs. Defining the height $h[k]$ of node k as

$$h[k] = \begin{cases} 1, & \text{if } k \in \mathscr{L}[r], \\ 1 + \max(h[l(k)], h[r(k)]), & \text{otherwise,} \end{cases} \tag{3}$$

we denote the set of all nodes in the binary tree of height h by $\mathscr{H}^h$:

$$\mathscr{H}^h = \{n \in \mathscr{D}[r] : h[n] = h\}\,. \tag{4}$$

Fig. 5 shows the node sets $\mathscr{H}^h$ for $h = 1, 5, 8$, and 9. The top most nodes in Figs. 3a and 3b belong to $\mathscr{H}^2$, and $\mathscr{H}^4$ of their respective binary trees.

The volume fractions of the grains (leaf nodes) relative to the polycrystalline aggregate, $w^{[k]}, k \in \mathscr{L}[r]$, such that $\sum_{k\in\mathscr{L}[r]} w^{[k]} = 1$, are inputs to the model. On their basis, each non-leaf node $n \in \mathscr{N}[r]$ may be assigned a volume fraction $w^{[n]} = w^{[l(n)]} + w^{[r(n)]} = \sum_{k\in\mathscr{L}[n]} w^{[k]}$. Also, we define

$$\rho^{[n]} = w^{[l(n)]}/(w^{[l(n)]} + w^{[r(n)]}), \tag{5}$$

to be the volume fraction of the sub-aggregate represented by node $l(n)$ relative to the sub-aggregate represented by non-leaf node n.

The higher nodes of the binary tree that represent sub-aggregates of grains are conceptual entities used in our model. However, the leaves of the binary tree represent the physical entities constituting the polycrystalline aggregate, viz., the grains. It is to these that we turn next.

2.2 Constitutive behavior of rate-independent grains

Consider a polycrystalline aggregate of N_g rigid-plastic rate-independent homogeneously deforming grains each of which accommodates an imposed volume-preserving strain-rate $\dot{\boldsymbol{\epsilon}}$, assumed uniform throughout the grain, by slip on crystallographic systems $s \in \{1, 2, \ldots, S\}$ with slip rates $\dot{\gamma}_s$. Following the Taylor-Bishop-Hill (Taylor, 1938, Bishop and Hill, 1951) formulation, this is expressed as

$$\dot{\boldsymbol{\epsilon}} = \sum_{s=1}^{S} \dot{\gamma}_s \boldsymbol{m}_s, \tag{6}$$

where, $\boldsymbol{m}_s$ denotes the symmetric Schmid tensor of the s-th slip system given by

$$\boldsymbol{m}_s = (\boldsymbol{b}_s \otimes \boldsymbol{n}_s + \boldsymbol{n}_s \otimes \boldsymbol{b}_s)/2. \tag{7}$$

$\boldsymbol{b}_s$ and $\boldsymbol{n}_s$ are the unit Burgers vector and unit normal vector, respectively, of slip system s. Following the convention of Chin and Mammel (1969) and Van Houtte and Aernoudt (1975a,b), we assume that $\dot{\gamma}_s \geq 0$, for all s. A slip system s is said to be active if $\dot{\gamma}_s > 0$.

Let the deviatoric part of the Cauchy stress, assumed uniform within the grain, be denoted by $\boldsymbol{\sigma}$. Then the resolved shear stress on the s-th slip system is $t_s = \boldsymbol{\sigma} : \boldsymbol{m}_s = \text{trace}\,(\boldsymbol{\sigma}\boldsymbol{m}_s)$. Schmid's law (Hosford, 1993) provides a condition for the activation of slip system s. Denoting the critical resolved shear stress of slip system s by τ_s, Schmid's law holds that

$$\dot{\gamma}_s \quad \begin{cases} = 0, & \text{if } t_s < \tau_s, \\ \geq 0, & \text{if } t_s = \tau_s, \\ \text{undefined}, & \text{if } t_s > \tau_s. \end{cases} \tag{8}$$

The plastic power of deformation, $\dot{W}$, is

$$\dot{W} = \sum_{s=1}^{S} \tau_s \dot{\gamma}_s = \sum_{i=1}^{3} \sum_{j=1}^{3} \sigma_{ij} \dot{\epsilon}_{ij}. \tag{9}$$

The second term in Eq. (9) is called the internal power and the third term is called the external power. Their equivalence was established by Chin and Mammel (1969).

It may be possible to satisfy Eq. (6) for fixed $\dot{\boldsymbol{\epsilon}}$, and fixed $\boldsymbol{m}_s$, using different combinations of $\dot{\gamma}_s$, with $\dot{\gamma}_s > 0$, for $s \in \mathscr{S} \subset \{1, 2, \ldots, S\}$, and $\dot{\gamma}_s = 0$, for $s \notin \mathscr{S}$. Taylor's principle (Hosford, 1993) asserts that the physically realized set of active slip systems $\mathscr{S}$ will be that which minimizes the internal plastic power subject to the constraints of Eqs. (6) and (8).

We take the evolution with deformation of the critical resolved shear stress, τ_s, to follow (Hill, 1966, Kocks et al., 1998)

$$\dot{\tau}_s = \frac{d\tau(\Gamma)}{d\Gamma} \sum_{s'=1}^{S} H_{ss'} \dot{\gamma}_{s'}, \tag{10}$$

where, $\underline{\underline{H}}$ is called the hardening matrix with $H_{ss} = 1$ for all $s \in \{1, \ldots, S\}$, and $\Gamma = \sum_{s=1}^{S} \gamma_s$ denotes the total shear strain accumulated in all the slip systems of the grain. $\tau(\Gamma)$ in Eq. (10) is taken to follow the extended Voce law of Tomé et al. (1984),

$$\tau(\Gamma) = \tau_0 + (\tau_1 + \theta_1 \Gamma)\left[1 - \exp(-\Gamma\theta_0/\tau_1)\right], \tag{11}$$

where τ_0, τ_1, θ_0, and θ_1 are taken to be material hardening constants.

In this work, we will apply the binary-tree based model to simulate large deformation of polycrystalline copper. The imposed deformation is assumed to be accommodated by slip within grains on one of $S = 24$ possible $\langle 110 \rangle (111)$ slip systems. We count opposite senses of slip directions on the same slip plane as different systems, consistent with the aforementioned assumption that $\dot{\gamma}_s \geq 0$. The hardening matrix, $\underline{H}$, assumed here incorporates the experimental observation of Franciosi and Zaoui (1982) that latent hardening of slip systems in copper is anisotropic and depends on the type of interaction between dislocations in the active and latent slip systems. The value of $H_{ss'}$, $s, s' \in \{1, \ldots, S\}$ is chosen depending upon whether the interaction between slip systems s and s' is of the self hardening ($H_{ss'} = h_0$), coplanar ($H_{ss'} = h_1$), colinear ($H_{ss'} = h_1$), Hirth locking ($H_{ss'} = h_1$), glissile junction forming ($H_{ss'} = h_2$), or Lomer-Cottrell junction forming ($H_{ss'} = h_3$) type, with strength increasing in that order, i.e., $1 = h_0 \leq h_1 \leq h_2 \leq h_3$. Furthermore, following Pierce et al. (1982) we taken $h_3 \leq 1.4$ in copper.

2.3 Kinematics of rigid-plastic rate-independent grains

The kinematics of slipping grains described below is well-established and is described, for example, in Asaro and Lubarda (2006), and Havner (1992). However, we summarize the relevant expressions here. The deformation gradient $\boldsymbol{F}$ of a rigid-plastic grain can be decomposed (Lee, 1969) as $\boldsymbol{F} = \boldsymbol{R}_{\text{lat}} \boldsymbol{F}_p$, where $\boldsymbol{R}_{\text{lat}}$ denotes an orthonormal tensor signifying lattice rotation, and $\boldsymbol{F}_p$ is the part of the deformation gradient accommodated through slip. The evolution of the deformation gradient is given by (e.g., Gurtin (1981))

$$\dot{\boldsymbol{F}} = \boldsymbol{L}\boldsymbol{F}, \tag{12}$$

where $\boldsymbol{L}$ denotes the velocity gradient of the grain. Rice (1971) related the evolution of $\boldsymbol{F}_p$ to slip through the flow rule

$$\dot{\boldsymbol{F}}_p = \boldsymbol{L}_p \boldsymbol{F}_p, \tag{13}$$

where,

$$\boldsymbol{L}_p = \sum_{s=1}^{S} \dot{\gamma}_s (\boldsymbol{R}_{\text{lat}}^T \boldsymbol{b}_s) \otimes (\boldsymbol{R}_{\text{lat}}^T \boldsymbol{n}_s) = \boldsymbol{R}_{\text{lat}}^T \left[\sum_{s=1}^{S} \dot{\gamma}_s \boldsymbol{b}_s \otimes \boldsymbol{n}_s \right] \boldsymbol{R}_{\text{lat}}. \tag{14}$$

$\boldsymbol{R}_{\text{lat}}^T \boldsymbol{b}_s$ and $\boldsymbol{R}_{\text{lat}}^T \boldsymbol{n}_s$ are the slip direction, and slip plane normal, respectively, of the s-th slip system in the reference configuration corresponding to $\boldsymbol{F} = \boldsymbol{F}_p = \boldsymbol{I}$. The term within square brackets in the last step of Eq. (14) is based on the orientation of the slip systems in the current (lattice rotated) configuration, and will occur more frequently in what follows. It is called the slip-rate

tensor (Fleck et al., 2003), and will denoted

$$\boldsymbol{L}_{\rm ss} = \sum_{s=1}^{S} \dot{\gamma}_s \boldsymbol{b}_s \otimes \boldsymbol{n}_s. \tag{15}$$

It is clear that $\boldsymbol{L}_p = \boldsymbol{R}_{\rm lat}^T \boldsymbol{L}_{\rm ss} \boldsymbol{R}_{\rm lat}$. The symmetric part of the slip rate, $\boldsymbol{L}_{\rm ss}$, is the strain-rate of the grain, $\dot{\boldsymbol{\epsilon}} = (\boldsymbol{L}_{\rm ss} + \boldsymbol{L}_{\rm ss}^T)/2$, according to Eq. (6).

The lattice rotation tensor $\boldsymbol{R}_{\rm lat}$ of a grain evolves as

$$\dot{\boldsymbol{R}}_{\rm lat} = \boldsymbol{W}_{\rm lat} \boldsymbol{R}_{\rm lat}, \tag{16}$$

where, $\boldsymbol{W}_{\rm lat}$ is skew-symmetric and is called the lattice spin tensor. The velocity gradient of the grain is comprised of contributions from slip rate, and lattice spin as

$$\boldsymbol{L} = \boldsymbol{L}_{\rm ss} + \boldsymbol{W}_{\rm lat}. \tag{17}$$

Taken together with Eqs. (12), (13), and (16), Eq. (17) implies (Pierce et al., 1983)

$$\boldsymbol{L} = \dot{\boldsymbol{F}} \boldsymbol{F}^{-1} = \boldsymbol{R}_{\rm lat} \dot{\boldsymbol{F}}_p \boldsymbol{F}_p^{-1} \boldsymbol{R}_{\rm lat}^T + \dot{\boldsymbol{R}}_{\rm lat} \boldsymbol{R}_{\rm lat}^T. \tag{18}$$

2.4 Kinematics of sub-aggregates in the binary-tree based model

We now extend the definitions of the kinematic quantities of grains in Sec. 2.3 to sub-aggregates. We take the velocity gradient of a sub-aggregate to be a volume fraction weighted average of the grains comprising it. That is, for the sub-aggregate represented by a node $n \in \mathscr{N}[r]$ in the binary tree,

$$\begin{aligned} \boldsymbol{L}^{[n]} &= \sum_{k \in \mathscr{L}[n]} \frac{w^{[k]}}{w^{[n]}} \boldsymbol{L}^{[k]} \\ &= \rho^{[n]} \boldsymbol{L}^{[l(n)]} + (1 - \rho^{[n]}) \boldsymbol{L}^{[r(n)]}. \end{aligned} \tag{19}$$

In view of the first step of Eq. (19), and Eq. (17), we may express $\boldsymbol{L}^{[n]}$ as

$$\boldsymbol{L}^{[n]} = \sum_{k \in \mathscr{L}[n]} \frac{w^{[k]}}{w^{[n]}} (\boldsymbol{L}_{\rm ss}^{[k]} + \boldsymbol{W}_{\rm lat}^{[k]}). \tag{20}$$

Note that since leaf nodes $k \in \mathscr{L}[n]$ in the binary tree represent grains, $\boldsymbol{L}_{\rm ss}^{[k]}$, and $\boldsymbol{W}_{\rm lat}^{[k]}$ in Eq. (20) are well-defined. Node $n \in \mathscr{N}[r]$ represents a sub-aggregate in the binary-tree based model, and as such, references to its lattice, slip directions, or slip plane normals are not meaningful. However, Eq. (20) suggests a formal definition of the slip rate and lattice spin for higher nodes

of the binary tree (representing sub-aggregates) that will prove valuable, viz.,

$$\begin{aligned}\boldsymbol{L}_{\text{ss}}^{[n]} &= \sum_{k\in\mathscr{L}[n]} \frac{w^{[k]}}{w^{[n]}}\boldsymbol{L}_{\text{ss}}^{[k]}, \\ &= \rho^{[n]}\boldsymbol{L}_{\text{ss}}^{[l(n)]} + (1-\rho^{[n]})\boldsymbol{L}_{\text{ss}}^{[r(n)]},\end{aligned} \tag{21}$$

and

$$\begin{aligned}\boldsymbol{W}_{\text{lat}}^{[n]} &= \sum_{k\in\mathscr{L}[n]} \frac{w^{[k]}}{w^{[n]}}\boldsymbol{W}_{\text{lat}}^{[k]}, \\ &= \rho^{[n]}\boldsymbol{W}_{\text{lat}}^{[l(n)]} + (1-\rho^{[n]})\boldsymbol{W}_{\text{lat}}^{[r(n)]},\end{aligned} \tag{22}$$

for $n \in \mathscr{N}[r]$. In view of the definitions in Eqs. (21) and (22), we may rewrite Eq. (20) as

$$\boldsymbol{L}^{[n]} = \boldsymbol{L}_{\text{ss}}^{[n]} + \boldsymbol{W}_{\text{lat}}^{[n]}. \tag{23}$$

For nodes $n \in \mathscr{N}[r]$ in the binary tree that represent sub-aggregates of grains, the tensors $\boldsymbol{L}_{\text{ss}}^{[n]}$, and $\boldsymbol{W}_{\text{lat}}^{[n]}$ are not derived from physical considerations of slip in the lattice. To emphasize this aspect, we will give quoted names to these quantities: 'slip-rate' for $\boldsymbol{L}_{\text{ss}}^{[n]}$ and 'lattice spin' for $\boldsymbol{W}_{\text{lat}}^{[n]}$. The 'strain-rate' in node $n \in \mathscr{N}[r]$ in the binary tree representation is then expressible as

$$\begin{aligned}\dot{\boldsymbol{\epsilon}}^{[n]} &= (\boldsymbol{L}_{\text{ss}}^{[n]} + \boldsymbol{L}_{\text{ss}}^{[n],T})/2 \\ &= \rho^{[k]}\dot{\boldsymbol{\epsilon}}^{[l(n)]} + (1-\rho^{[k]})\dot{\boldsymbol{\epsilon}}^{[r(n)]}, \\ &= \sum_{k\in\mathscr{L}[n]} \frac{w^{[k]}}{w^{[n]}}\dot{\boldsymbol{\epsilon}}^{[k]}.\end{aligned} \tag{24}$$

$\boldsymbol{L}^{[n]}$ determines the evolution of the deformation gradient $\boldsymbol{F}^{[k]}$ of the sub-aggregate represented by node n following

$$\dot{\boldsymbol{F}}^{[k]} = \boldsymbol{L}^{[k]}\boldsymbol{F}^{[k]}, \tag{25}$$

analogous to Eq. (12), and $\dot{\boldsymbol{W}}_{\text{lat}}^{[n]}$ likewise determines the evolution of the 'lattice rotation' of the sub-aggregate n:

$$\dot{\boldsymbol{R}}_{\text{lat}}^{[n]} = \dot{\boldsymbol{W}}_{\text{lat}}^{[n]}\boldsymbol{R}_{\text{lat}}^{[n]}, \tag{26}$$

analogous to Eq. (16). Finally, we specify that the plastic part of the deformation gradient of a sub-aggregate $n \in \mathscr{N}[r]$, $\dot{\boldsymbol{F}}_p^{[n]}$ evolves as $\dot{\boldsymbol{F}}_p^{[n]} = \boldsymbol{L}_p^{[n]}\boldsymbol{F}_p^{[n]}$, where $\boldsymbol{L}_p^{[n]} = \boldsymbol{R}_{\text{lat}}^{[n],T}\boldsymbol{L}_{\text{ss}}^{[n]}\boldsymbol{R}_{\text{lat}}^{[n]}$.

We have thus extended the definitions of all the kinematic variables defined for grains in the polycrystalline aggregate in Sec. 2.3 to arbitrary sub-aggregates, leaving the aforementioned kinematic variables well defined for every sub-aggregate in the binary-tree based model.

We will presently express a condition for velocity continuity between sub-aggregates represented by sibling nodes in the binary tree in terms of the kinematic quantities defined above. Let $\boldsymbol{\nu}^{[n]}$ denote the normal to the interface between the sub-aggregates represented by the children $l(n)$ and $r(n)$ of a node $n \in \mathscr{N}[r]$ in the binary tree. Hill (1961) has shown that the following condition is necessary for velocity continuity across the interface:

$$[\![\boldsymbol{L}^{[n]}]\!] := \boldsymbol{L}^{[r(n)]} - \boldsymbol{L}^{[l(n)]} = \boldsymbol{\lambda}^{[n]} \otimes \boldsymbol{\nu}^{[n]}, \tag{27}$$

for some vector $\boldsymbol{\lambda}^{[n]}$. := in Eq. (27), and elsewhere, indicates a definition (of $[\![\boldsymbol{L}^{[n]}]\!]$ in this case). Equating the symmetric parts of both sides of Eq. (27), we obtain

$$[\![\dot{\boldsymbol{\epsilon}}^{[n]}]\!] := \dot{\boldsymbol{\epsilon}}^{[r(n)]} - \dot{\boldsymbol{\epsilon}}^{[l(n)]} = (\boldsymbol{\lambda}^{[n]} \otimes \boldsymbol{\nu}^{[n]} + \boldsymbol{\nu}^{[n]} \otimes \boldsymbol{\lambda}^{[n]})/2, \tag{28}$$

as a necessary condition for velocity continuity across the interface with normal $\boldsymbol{\nu}^{[n]}$. It can be shown that (Mahesh, 2006)

$$\boldsymbol{\lambda}^{[n]} = 2[\![\dot{\boldsymbol{\epsilon}}^{[n]}]\!]\boldsymbol{\nu}^{[n]} - ([\![\dot{\boldsymbol{\epsilon}}^{[n]}]\!]\boldsymbol{\nu}^{[n]} \cdot \boldsymbol{\nu}^{[n]})\boldsymbol{\nu}^{[n]}, \tag{29}$$

whence it follows that $\boldsymbol{\lambda}^{[n]} \cdot \boldsymbol{\nu}^{[n]} = [\![\dot{\boldsymbol{\epsilon}}^{[n]}]\!]\boldsymbol{\nu}^{[n]} \cdot \boldsymbol{\nu}^{[n]} = 0$, since $[\![\dot{\boldsymbol{\epsilon}}^{[n]}]\!]$ is traceless.

Using Eq. (19), Eq. (27) may be rewritten in terms of slip rates and lattice spins as

$$(\boldsymbol{L}_{\text{ss}}^{[r(n)]} + \boldsymbol{W}_{\text{lat}}^{[r(n)]}) - (\boldsymbol{L}_{\text{ss}}^{[l(n)]} + \boldsymbol{W}_{\text{lat}}^{[l(n)]}) = \boldsymbol{\lambda}^{[n]} \otimes \boldsymbol{\nu}^{[n]}. \tag{30}$$

Additionally, imposing the average velocity gradient condition stated in the second step of Eq. (19), we have

$$\rho^{[n]}(\boldsymbol{L}_{\text{ss}}^{[l(n)]} + \boldsymbol{W}_{\text{lat}}^{[l(n)]}) + (1 - \rho^{[n]})(\boldsymbol{L}_{\text{ss}}^{[r(n)]} + \boldsymbol{W}_{\text{lat}}^{[r(n)]}) = \boldsymbol{L}^{[n]}. \tag{31}$$

Eqs. (30), and (31) may be solved to obtain

$$\begin{aligned} \boldsymbol{W}_{\text{lat}}^{[l(n)]} &= \text{skew}\left\{(\boldsymbol{L}^{[n]} - \boldsymbol{L}_{ss}^{[n]}) - (1 - \rho^{[n]})(\boldsymbol{\lambda}^{[n]} \otimes \boldsymbol{\nu}^{[n]} - [\![\boldsymbol{L}^{[n]}]\!])\right\}, \text{ and} \\ \boldsymbol{W}_{\text{lat}}^{[r(n)]} &= \text{skew}\left\{(\boldsymbol{L}^{[n]} - \boldsymbol{L}_{ss}^{[n]}) + \rho^{[n]}(\boldsymbol{\lambda}^{[n]} \otimes \boldsymbol{\nu}^{[n]} - [\![\boldsymbol{L}^{[n]}]\!])\right\}, \end{aligned} \tag{32}$$

for the 'lattice spins' in the left and right child of node n. Eqs. (28) and (32) thus express the velocity continuity conditions across the interface between children of node n in the binary-tree based model.

2.6 Traction continuity

Following Bishop and Hill (1951), Hill (1967), and Havner (1971), we take the deviatoric part of the Cauchy stress of a sub-aggregate represented by node

$n \in \mathscr{N}[r]$ in the binary tree as a volume average over its constituent grains

$$\begin{aligned} \boldsymbol{\sigma}^{[n]} &= \sum_{k \in \mathscr{L}[n]} \frac{w^{[k]}}{w^{[n]}} \boldsymbol{\sigma}^{[k]}, \\ &= \rho^{[n]} \boldsymbol{\sigma}^{[l(n)]} + (1 - \rho^{[n]}) \boldsymbol{\sigma}^{[r(n)]}. \end{aligned} \tag{33}$$

Traction continuity across an interface with normal $\boldsymbol{\nu}^{[n]}$ requires

$$(\boldsymbol{\sigma}^{[r(n)]} - \boldsymbol{\sigma}^{[l(n)]}) \boldsymbol{\nu}^{[n]} = \mathbf{0}. \tag{34}$$

2.7 Boundary conditions

The full constraints (Kocks et al., 1998) form of the boundary condition imposed on the root node r of the binary tree representation of the model is

$$\boldsymbol{L}^{[r]} = \boldsymbol{L}^{\text{imp}}, \tag{35}$$

where $\boldsymbol{L}^{\text{imp}}$ is a prescribed traceless tensor. Using Eqs. (23) and (24), we see that Eq. (35) implies

$$\dot{\boldsymbol{\epsilon}}^{[r]} = \dot{\boldsymbol{\epsilon}}^{\text{imp}}, \tag{36}$$

where $\dot{\boldsymbol{\epsilon}}^{\text{imp}} = (\boldsymbol{L}^{\text{imp}} + \boldsymbol{L}^{\text{imp},T})/2$. Imposition of the skew part of $\boldsymbol{L}^{[r]}$ will be considered in Sec. 2.10. Relaxed constraints boundary conditions (Honneff and Mecking, 1978) entail leaving some of the components of $\dot{\boldsymbol{\epsilon}}^{\text{imp}}$ unspecified.

2.8 Continuity and boundary conditions expressed in component form

We now express the strain-rate compatibility condition, Eq. (28), traction continuity condition, Eq. (34), and boundary condition, Eq. (36) in component form. We denote matrices by an underlined symbol, e.g., $\underline{T}$, and the matrix representation of a tensor $\boldsymbol{T}$ in a coordinate system (xyz) by $[\boldsymbol{T}]_{(xyz)}$ in the following.

It will be convenient to express the velocity and traction continuity conditions in the Leibfried-Breuer notation (Lebensohn et al., 1998b) given relative to five symmetric traceless basis matrices $\{\underline{b}_\lambda : \lambda \in \{1, \ldots, 5\}\}$ that obey the orthonormality condition $\underline{b}_\lambda : \underline{b}_\mu = \delta_{\lambda\mu}$, and that span the space of traceless symmetric matrices. The λ-th component of the Leibfried-Breuer vector representation of a traceless symmetric 3×3 matrix $\underline{T}$ is $T_\lambda = \underline{T} : \underline{b}_\lambda$, and the components are given by

$$(T_1, \ldots, T_5) = \left(\frac{T_{22} - T_{11}}{\sqrt{2}}, \frac{2T_{33} - T_{11} - T_{22}}{\sqrt{6}}, \sqrt{2}T_{23}, \sqrt{2}T_{13}, \sqrt{2}T_{12} \right). \tag{37}$$

Let $(xyz)_1$ and $(xyz)_2$ be two orthonormal coordinate systems rotated relative to each other. Let the matrix representation of a tensor $\boldsymbol{T}$ in $(xyz)_1$ and $(xyz)_2$ be related through $[\boldsymbol{T}]_{(xyz)_1} = \underline{R}^T [\boldsymbol{T}]_{(xyz)_2} \underline{R}$, where $\underline{R}$ is an orthonormal matrix. Then, it can be shown that there exists an orthonormal 5×5 matrix $\underline{\alpha}$, whose components are given by

$$\alpha_{\lambda\mu} = \underline{R}^T \underline{b}_\mu \underline{R} : \underline{b}_\lambda, \tag{38}$$

such that $[T_\lambda]_{(xyz)_1} = \sum_{\mu=1}^{5} \alpha_{\lambda\mu} [T_\mu]_{(xyz)_2}$. $\underline{\alpha}$ is thus a rotation matrix that effects basis rotations in the space of Leibfried-Breuer vectors.

Let XYZ be a sample fixed Cartesian reference frame. Associated with each interface $n \in \mathscr{N}[r]$ in the binary tree representation of the polycrystal, we define an interfacial reference frame $(xyz)^{[n]}$ such that $y^{[n]}$ coincides with the normal $\boldsymbol{\nu}^{[n]}$. In the $(xyz)^{[n]}$ coordinate system fixed to the interface, the compatibility condition, Eq. (28), is

$$\begin{aligned} \dot{\epsilon}_{11}^{l(n)} &= \dot{\epsilon}_{11}^{r(n)}, \\ \dot{\epsilon}_{33}^{l(n)} &= \dot{\epsilon}_{33}^{r(n)}, \\ \dot{\epsilon}_{13}^{l(n)} &= \dot{\epsilon}_{13}^{r(n)}, \end{aligned} \tag{39}$$

and the traction continuity condition of Eq. (34) becomes

$$\begin{aligned} \sigma_{12}^{l(n)} &= \sigma_{12}^{r(n)}, \\ \sigma_{23}^{l(n)} &= \sigma_{23}^{r(n)}. \end{aligned} \tag{40}$$

In Leibfried-Breuer notation, Eqs. (39) and (40) expressing compatibility in the $(xyz)^{[n]}$ coordinate system can be written as

$$\begin{aligned} \dot{\epsilon}_1^{l(n)} &= \dot{\epsilon}_1^{r(n)}, \\ \dot{\epsilon}_2^{l(n)} &= \dot{\epsilon}_2^{r(n)}, \\ \sigma_3^{l(n)} &= \sigma_3^{r(n)}, \\ \dot{\epsilon}_4^{l(n)} &= \dot{\epsilon}_4^{r(n)}, \text{ and} \\ \sigma_5^{l(n)} &= \sigma_5^{r(n)}, \end{aligned} \tag{41}$$

which are the same as the continuity conditions assumed by Lebensohn et al. (1998a) in a twinning grain. Suppose $\underline{R}$ represents a rotation between the XYZ and $(xyz)^{[n]}$ coordinate systems so that $[\boldsymbol{T}]_{(xyz)^{[n]}} = \underline{R}^T [\boldsymbol{T}]_{XYZ} \underline{R}$, for any tensor $\boldsymbol{T}$. Basis rotation using the 5×5 rotation matrix $\underline{\alpha}^{[n]}$, given by Eq. (38), transforms Eqs. (41) into the sample XYZ coordinate system as

$$\sum_{q=1}^{5} S_{pq}^{[n]} (\dot{\epsilon}_q^{[r(n)]} - \dot{\epsilon}_q^{[l(n)]}) = 0, \tag{42}$$

where,

$$\underline{S}^{[n]} = \begin{pmatrix} 1\,0\,0\,0\,0 \\ 0\,1\,0\,0\,0 \\ 0\,0\,0\,1\,0 \end{pmatrix} \underline{\alpha}^{[n]}, \tag{43}$$

and,

$$\sum_{q=1}^{5} T_{pq}^{[n]} (\sigma_q^{[r(n)]} - \sigma_q^{[l(n)]}) = 0, \tag{44}$$

where,

$$\underline{T}^{[n]} = \begin{pmatrix} 0\,0\,1\,0\,0 \\ 0\,0\,0\,0\,1 \end{pmatrix} \underline{\alpha}^{[n]}. \tag{45}$$

Eqs. (42) and (44) are a restatement, in matrix form, of Eqs. (28) and (34), respectively.

Following the same reasoning that led to Eq. (42), the boundary condition given by Eq. (36) with some of constraints relaxed can be written in the form

$$\sum_{q=1}^{5} S_{pq} \dot{\epsilon}_q^{[r]} = U_p, \tag{46}$$

where, $\underline{U}$ is a vector whose components are determined only by those Leibfried-Breuer components of $\boldsymbol{\epsilon}^{\text{imp}}$ that are not relaxed. Mahesh (2009) has discussed the expression of several common types of boundary conditions in the form of Eq. (46).

2.8.1 Other types of continuity across interfaces

To make contact with some of the existing models of polycrystal plasticity it will prove advantageous to consider a class of velocity and traction continuity constraints between sibling nodes that includes Eqs. (42–45) as a special case. To this end, we assume that a set $\mathscr{P}^{[n]} \subset \{1, 2, 3, 4, 5\}$ is specified at each node $n \in \mathscr{N}[r]$. $\mathscr{P}^{[n]}$ determines the continuity conditions between the children of node n according to

$$\begin{aligned} \dot{\epsilon}_p^{l(n)} &= \dot{\epsilon}_p^{r(n)}, \text{ if } p \in \mathscr{P}^{[n]}, \text{ and} \\ \sigma_p^{l(n)} &= \sigma_p^{r(n)}, \text{ if } p \notin \mathscr{P}^{[n]}, \end{aligned} \tag{47}$$

in the $(xyz)^{[n]}$ coordinate system.

Evidently, if $\mathscr{P}^{[n]} = \{1, 2, 4\}$, we retrieve the continuity conditions given by Eqs. (42–45). Restricting attention to binary trees of the form shown in Fig. 3a, we find this model is the same as that of Lebensohn et al. (1998a), Lebensohn

(1999), Van Houtte et al. (1999), and the Taylor bicrystal model of Lee et al. (2002). Further, the case of the Taylor model obtains if $\mathscr{P}^{[n]} = \{1, 2, 3, 4, 5\}$ for all $n \in \mathscr{N}[r]$. If, on the other hand, $\mathscr{P}^{[n]} = \emptyset$, and we restrict attention to binary trees of the form shown in Fig. 3a, we get the Sachs bicrystal model of Lee et al. (2002). Likewise, if $\mathscr{P}^{[n]} = \emptyset$, and we restrict attention to the binary trees of the form shown in Fig. 3b, we get a version of the GIA model of Engler et al. (2005), with no energy associated with the geometrically necessary dislocation needed to accommodate intergranular incompatibility.

It is clear that by making different choices for $\mathscr{P}^{[n]}$, $n \in \mathscr{N}[r]$, a vast family of different models of the polycrystalline aggregate can be constructed.

2.9 Problem statement, and reduction to a linear program

The problem under consideration in this section is as follows: Given a binary-tree based model (developed perhaps from a micrograph as shown in Sec. 1), and given a macroscopic strain-rate $\dot{\boldsymbol{\epsilon}}^{[r]}$ imposed on its root node r, determine the slip rates

$$\left\{\dot{\gamma}_s^{[k]} \geq 0 : s \in \{1, 2, \ldots S\};\ k \in \mathscr{L}[r]\right\}$$

in each grain such that (i) strain-rate compatibility prescribed by Eq. (28) between sibling nodes holds, (ii) traction continuity given by Eq. (34) is maintained between all sibling nodes in the binary tree, and (iii) $\dot{\gamma}_s^{[k]}$ in each grain k is such that the constraint of Eq. (8), and the minimization of plastic power in each grain given by Eq. (9) are satisfied.

The central result proved in this section is that the optimum set of slip rates will be one that minimizes the plastic power of the entire polycrystal,

$$\dot{W}(\underline{\dot{\gamma}}) = \sum_{k \in \mathscr{L}[r]} \frac{w^{[k]}}{w^{[r]}} \sum_{s=1}^{S} \tau_s^{[k]} \dot{\gamma}_s^{[k]}, \tag{48}$$

obtained as the volume fraction weighted sum of the plastic power of individual grains, subject only to the constraint (i), and not explicitly to (ii) and (iii). Furthermore, the minimization can be expressed as a linear programming problem, which is amenable to numerical solution by standard techniques (Dantzig, 1963). Recall from Sec. 2.2 that $\dot{\gamma}_s^{[k]} \geq 0$, and $\tau_s^{[k]} > 0$.

Consider minimizing the plastic power of a polycrystal, given by Eq. (48), subject to the constraints

$$\begin{aligned} f_p(\underline{\dot{\gamma}}) &= 0, \text{ for } p \in \mathscr{P} \text{ and,} \\ g_p^{[n]}(\underline{\dot{\gamma}}) &= 0, \text{ for } n \in \mathscr{N}[r],\ p \in \mathscr{P}^{[n]}. \end{aligned} \tag{49}$$

Here, $f_p(\underline{\dot{\gamma}}) = 0$ sets the imposed deformation upon the root node r of the binary tree (representing the entire polycrystalline aggregate) given by Eq. (46), and $g_p^{[n]}(\underline{\dot{\gamma}}) = 0$ sets velocity continuity given by Eq. (42) between the children of node n in the binary tree, which represent two sub-aggregates.

Using Eq. (46) we write

$$\begin{aligned} f_p(\underline{\dot{\gamma}}) &= U_p - \sum_{q=1}^{5} S_{pq}\dot{\epsilon}_q^{[r]} \\ &= U_p - \sum_{k\in\mathscr{L}[r]} \frac{w^{[k]}}{w^{[r]}} \sum_{s=1}^{S}\sum_{q=1}^{5} S_{pq} m_{qs}^{[k]} \dot{\gamma}_s^{[k]}, \end{aligned} \tag{50}$$

and using Eq. (42) we express $g_p^{[n]}(\underline{\dot{\gamma}})$ as

$$\begin{aligned} g_p^{[n]}(\underline{\dot{\gamma}}) &= \sum_{q=1}^{5} S_{pq}^{[n]} (\dot{\epsilon}_q^{[r(n)]} - \dot{\epsilon}_q^{[l(n)]}) \\ &= \sum_{q=1}^{5} S_{pq}^{[n]} \left\{ \sum_{k\in\mathscr{L}[r(n)]} \frac{w^{[k]}}{w^{[r(n)]}} \sum_{s=1}^{S} m_{qs}^{[k]} \dot{\gamma}_s^{[k]} - \sum_{k\in\mathscr{L}[l(n)]} \frac{w^{[k]}}{w^{[l(n)]}} \sum_{s=1}^{S} m_{qs}^{[k]} \dot{\gamma}_s^{[k]} \right\}. \end{aligned} \tag{51}$$

The second step in Eqs. (50) and (51) follows from substituting for strain-rates using Eqs. (24) and (6) in the corresponding first steps. Note that neither (i) the traction continuity conditions nor (ii) the constitutive constraints imposed on the grain by Eq. (8) have been invoked in the constrained-minimization problem stated above. In fact, stresses do not figure in the statement of the stated constrained-minimization problem, and are a part of its solution, as we now show.

The Lagrangian of this constrained-minimization problem is

$$F(\underline{\dot{\gamma}}, \underline{\lambda}, \underline{\mu}) = \dot{W}(\underline{\dot{\gamma}}) + \sum_{p\in\mathscr{P}} \lambda_p f_p(\underline{\dot{\gamma}}) + \sum_{n\in\mathscr{N}[r]} \sum_{p\in\mathscr{P}^{[n]}} \mu_p^{[n]} g_p^{[n]}(\underline{\dot{\gamma}}), \tag{52}$$

where λ_p and $\mu_p^{[n]}$ are the Lagrange multipliers of the constraints in Eq. (49). Following the notation of Chin and Mammel (1969), $\underline{\dot{\gamma}}$ denotes an array comprising of all the slip rates, and $\underline{\lambda}$ and $\underline{\mu}$ denote arrays comprising of the Lagrange multipliers in the model. The linearity of the objective and constraint functions in $\underline{\dot{\gamma}}$ allows the application of the Karush-Kuhn-Tucker conditions (Rockafellar, 1970) that identifies the saddle point of $F(\underline{\dot{\gamma}}, \underline{\lambda}, \underline{\mu})$ by the condition:

$$\frac{\partial F}{\partial \dot{\gamma}_s^{[k]}} \begin{cases} = 0, & \text{if } \dot{\gamma}_s^{[k]} > 0 \text{ and,} \\ \geq 0, & \text{if } \dot{\gamma}_s^{[k]} = 0, \end{cases} \tag{53}$$

for $k \in \mathscr{L}[r]$. Substituting the Lagrangian, Eq. (52) into Eq. (53) and simpli-

fying, we obtain

$$\tau_s^{[k]} = \sum_{q=1}^{5} \varsigma_q^{[k]} m_{qs}^{[k]}, \tag{54}$$

provided $\dot{\gamma}_s^{[k]} > 0$, where,

$$\varsigma_q^{[k]} = \sum_{p\in\mathscr{P}} \lambda_p S_{pq} + \sum_{n\in\mathscr{N}[r]} \sum_{p\in\mathscr{P}^{[n]}} \mu_p^{[n]} S_{pq}^{[n]} \left[\frac{\mathbf{1}_{[k\in\mathscr{D}[r(n)]]}}{w^{[r(n)]}} - \frac{\mathbf{1}_{[k\in\mathscr{D}[l(n)]]}}{w^{[l(n)]}} \right]. \tag{55}$$

for $q \in \{1, \ldots, 5\}$. $\mathbf{1}_{[A]}$, the indicator of A, equals 1 if A is satisfied, and 0 if not. Comparing Eqs. (54) and (8) we realize that we must have $\varsigma_q^{[k]} = \sigma_q^{[k]}$, so that,

$$\sigma_q^{[k]} = \sum_{p\in\mathscr{P}} \lambda_p S_{pq} + \sum_{n\in\mathscr{A}[k]} \sum_{p\in\mathscr{P}^{[n]}} \mu_p^{[n]} S_{pq}^{[n]} \left[\frac{\mathbf{1}_{[k\in\mathscr{D}[r(n)]]}}{w^{[r(n)]}} - \frac{\mathbf{1}_{[k\in\mathscr{D}[l(n)]]}}{w^{[l(n)]}} \right], \tag{56}$$

where we have replaced $\mathscr{N}[r]$ by $\mathscr{A}[k]$ (defined in Sec. 2.1) since the contribution of the nodes comprising $\mathscr{N}[r] - \mathscr{A}[k]$ to the sum in the second term of the right side of Eq. (56) is zero. Eq. (56) is an expression for the grain level deviatoric part of the Cauchy stress components expressed in Leibfried-Breuer notation. Using Eq. (56), and Eq. (33), we can find the stress in an arbitrary node of the binary tree by proceeding sequentially up the tree, from leaves to root. For instance, the deviatoric Cauchy stress components in the parent node $k = p(k_1) = p(k_2)$ of two leaf nodes $k_1 \in \mathscr{L}[r]$, and $k_2 \in \mathscr{L}[r]$ is obtained using Eq. (33) as

$$\begin{aligned} \sigma_q^{[k]} =& \frac{w^{[k_1]}}{w^{[k_1]} + w^{[k_2]}} \sigma_q^{[k_1]} + \frac{w^{[k_2]}}{w^{[k_1]} + w^{[k_2]}} \sigma_q^{[k_1]}, \\ =& \sum_{p\in\mathscr{P}} \lambda_p S_{pq} + \sum_{n\in\mathscr{A}[k]} \sum_{p\in\mathscr{P}^{[n]}} \mu_p^{[n]} S_{pq}^{[n]} \left[\frac{\mathbf{1}_{[k\in\mathscr{D}[r(n)]]}}{w^{[r(n)]}} - \frac{\mathbf{1}_{[k\in\mathscr{D}[l(n)]]}}{w^{[l(n)]}} \right]. \end{aligned} \tag{57}$$

The form of the Leibfried-Breuer components of the deviatoric Cauchy stress given in the second step of Eq. (57) for a non-leaf parent node, which represents a sub-aggregate of two grains, is thus identical to that given in Eq. (56) for grains. Continuing this argument inductively shows that Eq. (57) is valid for any node $k \in \mathscr{D}[r]$ in the binary tree representing a sub-aggregate in the binary-tree based model.

It was remarked that the statement of the constrained-minimization problem involved no explicit constraints requiring traction continuity between sub-aggregates represented by siblings in the binary tree. It remains to show that these continuity conditions are indeed satisfied by the solution for the deviatoric part of the Cauchy stress in Eq. (57). To this end, consider the case that the XYZ and $(xyz)^{[n]}$ coordinate systems, defined in Sec. 2.8, coincide for some $n \in \mathscr{N}[r]$. Then, the compatibility constraints $g_p^{[n]}(\underline{\dot{\gamma}}) = 0$ in Eq. (49) reduce to $\dot{\epsilon}_p^{[l(n)]} = \dot{\epsilon}_p^{[r(n)]}$, for $p \in \mathscr{P}^{[n]}$. More remarkably, for $p \notin \mathscr{P}^{[n]}$, Eq. (57)

implies that

$$\sigma_q^{[l(n)]} = \sigma_q^{[r(n)]} = \sigma_q^{[n]} = \sum_{p\in\mathscr{P}} \lambda_p S_{pq} + \sum_{m\in\mathscr{A}[n]} \sum_{p\in\mathscr{P}^{[m]}} \mu_p^{[m]} S_{pq}^{[m]} \left[\frac{\mathbf{1}_{[n\in\mathscr{D}[r(m)]]}}{w^{[r(m)]}} - \frac{\mathbf{1}_{[n\in\mathscr{D}[l(m)]]}}{w^{[l(m)]}} \right]. \tag{58}$$

Thus, we have the key property that the solution of the linear programming problem automatically satisfies traction continuity given by Eq. (44). This result may be considered an extension to the binary-tree based polycrystal of Taylor's principle (Hosford, 1993, Kocks et al., 1998) originally stated for a grain (see Sec. 2.2): Of all possible $\underline{\dot{\gamma}}$ capable of accommodating the deformation imposed on a binary-tree based polycrystal, the physically realized set of grain slips will be that which minimizes the internal plastic power $\dot{W}(\underline{\dot{\gamma}})$ (Eq. (48)) of the polycrystal subject to the constraints of Eq. (49).

If these considerations are applied to the two grain binary-tree based model shown in Fig. 3a, we find that the shear traction components on the grain boundary between the grains A and B must be continuous. This result was first shown by Van Houtte et al. (1999) for their LAMEL model.

The constraints of Eq. (49b) become void if $\mathscr{P}^{[n]} = \emptyset$ for all $n \in \mathscr{N}[r]$. In this case, the binary-tree based polycrystal predicts a uniform Cauchy stress in all the grains, and is equivalent to the Sachs polycrystal. On the other hand, if $\mathscr{P}^{[n]} = \{1, 2, 3, 4, 5\}$, the constraints of Eq. (49) fully determine $\underline{\dot{\gamma}}$, and we have the Taylor model. It is well known (Kocks et al., 1998) that the Sachs and Taylor models predict the lower and upper bounds of the plastic power $\dot{W}(\underline{\dot{\gamma}})$, respectively. This gives us an interpretation of the binary-tree based model as a means to span the gamut of polycrystal responses from lower bound Sachs to upper bound Taylor, depending on the selection of $\mathscr{P}^{[n]}$, $n \in \mathscr{N}[r]$.

Eqs. (48) and (49) constitute a linear programming problem that can be solved using standard methods (Dantzig, 1963). Eq. (57) provides an expression for the deviatoric part of the Cauchy stress in the nodes of the binary tree in terms of the Lagrange multipliers enforcing the constraints.

The linear program given by Eqs. (48) and (49) may admit multiple solutions. To each solution variable in a linear program, corresponds a so-called reduced cost (Dantzig, 1963). Non-uniqueness of the solution is indicated when zero reduced cost values are associated with zero valued solution variables.

In solving for the slip-rates in a single grain, Van Houtte and Aernoudt (1975a,b) took the mean of all the extreme solutions of the linear programming problem. Based on comparisons with experimental observations, Fuh and Havner (1989) proposed the minimum plastic spin criterion, which asserts that subject to all the constraints and critical slip-system inequalities, slip rates are selected so as to minimize the relative spin between material and lattice. While the procedure of Van Houtte and Aernoudt (1975a,b) has no

physical justification, the criterion of Fuh and Havner (1989) does not readily extend to aggregates of grains, as required in the binary tree based model. Therefore, in the following, when the linear program of Eqs. (48) and (49) has multiple solutions, we select one of the possible solutions at random.

Once the set of all $\left\{\dot{\gamma}_s^{[k]} : s \in \{1, 2, \dots S\};\ k \in \mathscr{L}[r]\right\}$ are determined, kinematic quantities such as $\boldsymbol{L}_{\text{ss}}^{[k]}$, for all grains $k \in \mathscr{L}[r]$, using Eq. (15), and $\boldsymbol{L}_{\text{ss}}^{[n]}$, for all sub-aggregates $n \in \mathscr{N}[r]$, using Eq. (21), can be found.

2.10 Lattice rotations

The 'lattice spin' $\boldsymbol{W}_{\text{lat}}^{[r]}$ of the root node of the binary tree, which represents the entire polycrystalline aggregate, must be set so as to satisfy the boundary condition given by Eq. (35). According to Eq. (23) with $n = r$, this implies $\boldsymbol{L}^{[r]} = \boldsymbol{L}_{\text{ss}}^{[r]} + \boldsymbol{W}_{\text{lat}}^{[r]} = \boldsymbol{L}^{\text{imp}}$, so that

$$\boldsymbol{W}_{\text{lat}}^{[r]} = \text{skew}(\boldsymbol{L}^{\text{imp}} - \boldsymbol{L}_{\text{ss}}^{[r]}). \tag{59}$$

With the 'lattice spin' $\boldsymbol{W}_{\text{lat}}^{[r]}$ of the polycrystalline aggregate represented by the root node r thus determined, the lattice spins $\boldsymbol{W}_{\text{lat}}^{l(r)}$, and $\boldsymbol{W}_{\text{lat}}^{r(r)}$ of the sub-aggregates represented by the nodes $l(r)$, and $r(r)$ of the binary tree can be calculated using Eq. (32). Continuing this procedure one can calculate the 'lattice spin' of all sub-aggregates, including that of the grains. The lattice spins of grains can then be used to update their lattice orientations following standard procedures (Kocks et al., 1998).

We reiterate a point made in Sec. 2.4 that non-leaf nodes $n \in \mathscr{N}[r]$ represent sub-aggregates in the binary-tree based model, and references to their lattice spins are not physically meaningful. However, as shown presently, this definition results in a consistent formula for the physically meaningful lattice spin of grains.

2.11 Evolution equations and time integration

Following an extension of the notions implicit in Van Houtte and Aernoudt (1975b), we may express the state of the binary-tree based polycrystal by $\{\underline{\gamma}, \underline{R}, \underline{\tau}\}$. Here, $\underline{\gamma} = \{\gamma_s^{[k]} \geq 0 : s \in \{1, 2, \dots S\};\ k \in \mathscr{L}[r]\}$ denotes the set of accumulated slips in each grain of the polycrystal, $\underline{\boldsymbol{R}} = \{\boldsymbol{R}_{\text{lat}}^{[k]} :\ k \in \mathscr{L}[r]\}$ denotes the lattice orientations of each grain in the polycrystal, and $\underline{\tau} = \{\tau_s^{[k]} \geq 0 : s \in \{1, 2, \dots S\};\ k \in \mathscr{L}[r]\}$ denotes the set of critical resolved shear stresses of each slip system of each grain of the polycrystal. The foregoing

sections have constructed a set of evolution equations for the state that can be expressed as

$$\left\{ \begin{array}{c} \dot{\underline{\gamma}} \\ \dot{\underline{\underline{\boldsymbol{R}}}} \\ \dot{\underline{\tau}} \end{array} \right\} = f \left(\left\{ \begin{array}{c} \underline{\gamma} \\ \underline{\underline{\boldsymbol{R}}} \\ \underline{\tau} \end{array} \right\} \right) . \tag{60}$$

Sec. 2.9 connects $\dot{\underline{\gamma}} = f_1(\underline{\theta}, \underline{\tau})$; Eqs. (16) and (32) relate $\dot{\underline{\underline{\boldsymbol{R}}}} = g_2(\underline{\underline{\boldsymbol{R}}}, \dot{\underline{\gamma}}) = g_2(\underline{\underline{\boldsymbol{R}}}, f_1(\underline{\underline{\boldsymbol{R}}}, \underline{\tau})) = f_2(\underline{\underline{\boldsymbol{R}}}, \underline{\tau})$; and Eqs. (10) and (11) relate $\dot{\underline{\tau}} = g_3(\underline{\gamma}, \dot{\underline{\gamma}}) = g_3(\underline{\gamma}, f_1(\underline{\theta}, \underline{\tau})) = f_3(\underline{\gamma}, \underline{\theta}, \underline{\tau})$. f, f_1, f_2, f_3, g_2, and g_3 are functions whose explicit or implicit forms have been defined in the preceding sections.

As given by Eq. (60), the evolution equations are amenable to numerical integration in time to follow the evolving state of the binary-tree based polycrystal.

3 Results and discussion

We will now study the predictions and computational time performance of the present model applied to polycrystalline copper. In this study, we treat the various rate-dependent binary-tree based models studied in I as benchmarks. We recall that in the rate-dependent model, the relationship between the slip-rate in slip system s in grain $k \in \mathscr{L}[r]$ and the deviatoric part of the Cauchy stress $\boldsymbol{\sigma}^{[k]}$ therein is (Hutchinson, 1976, Asaro and Needleman, 1985)

$$\dot{\gamma}_s^{[k]} = |\boldsymbol{\sigma}^{[k]} : \boldsymbol{m}_s / \tau_s|^n \ \text{sign} \left(\boldsymbol{\sigma}^{[k]} : \boldsymbol{m}_s \right) , \tag{61}$$

where $\boldsymbol{m}_s$ was defined in Sec. 2.2, and n is the reciprocal rate-sensitivity. The rate-independent limit corresponds to $n \to \infty$.

To aid comparison with I, the starting random texture of $N_g = 256$ grains used in the present study is the same as that in I. The structure of the balanced binary tree formed by the $N_g = 256$ grains and $2N_g - 1 = 511$ nodes, is shown schematically in Fig. 5, and is identical to that in I. As in I, we also study the effect of imposed deformation at nodes of different heights in the binary tree. Specifically, we will study deformations imposed upon the elements of node sets $\mathscr{H}^1$, $\mathscr{H}^5$, and $\mathscr{H}^9$ (Eqs. (4) and (46), and Fig. 5). We will refer to the models with deformation imposed upon $\mathscr{H}^5$ or $\mathscr{H}^9$ as *true binary-tree based models*. When deformation is imposed upon $\mathscr{H}^1$, the binary-tree based model reduces to the classical Taylor model.

Grains harden in the present simulations following the extended Voce hardening law of Tomé et al. (1984) stated in Sec. 2.2. The Voce hardening parameters are listed in Table 1 for the rate-independent model. The latent hardening coefficients h_1, h_2, and h_3 are fit to approximately match the predicted textures

Table 1
Voce parameters (in MPa) used in fitting Tomé et al. (1984)'s experimental stress strain curves using the rate-independent binary-tree based model. The hardening constants are $h_0 = 1.0$, $h_1 = 1.0$, $h_2 = 1.2$, and $h_3 = 1.2$.

Loading	τ_0	θ_0	τ_1	θ_1
Tension	15	210	110	6
Compression	15	210	110	2
Torsion	15	250	100	3

with the experimental textures of Hirsch and Lucke (1988a) after rolling deformation, and the hardening parameters τ_0, θ_0, τ_1, and θ_1 are fit to match the experimental stress-strain curves in tension, compression, and torsion reported by Tomé et al. (1984) using the $\mathscr{H}^9$ model. The same parameters are then used in the simulations with loading imposed on $\mathscr{H}^5$, and $\mathscr{H}^1$.

As stated in Sec. 2.2, the present study assumes rigid-plastic grain response. This assumption has been found to result in almost the same predictions as that of elasto-plastic grain response, when applied to simulate deformation processes to strains well beyond the elastic limit (Saran, 1991). Since the simulations studies reported below go up to von Mises strains of 1, which lies well outside the elastic limit, the neglect of elasticity is expected to have no significant effect on the predictions.

3.1 Stress-strain response in tension, compression and torsion

The binary-tree based model is subjected to tension and compression along the Z direction by imposing on the root node r, velocity gradient given by

$$[\boldsymbol{L}^{[r]}]_{XYZ} = \begin{pmatrix} \cdot & \cdot & 0 \\ \cdot & \cdot & 0 \\ 0 & 0 & \pm 1 \end{pmatrix}, \tag{62}$$

where constraints on $L_{ij}^{[r]}$ $(i, j \in \{1, 2\})$ are left unspecified, i.e., relaxed. $L_{33}^{[r]} = 1$ corresponds to tension, and $L_{33}^{[r]} = -1$ to compression. Torsion is imposed by setting

$$[\boldsymbol{L}^{[r]}]_{XYZ} = \begin{pmatrix} 0 & 0 & 1 \\ 0 & 0 & 0 \\ 0 & 0 & 0 \end{pmatrix}, \tag{63}$$

with no constraints relaxed.

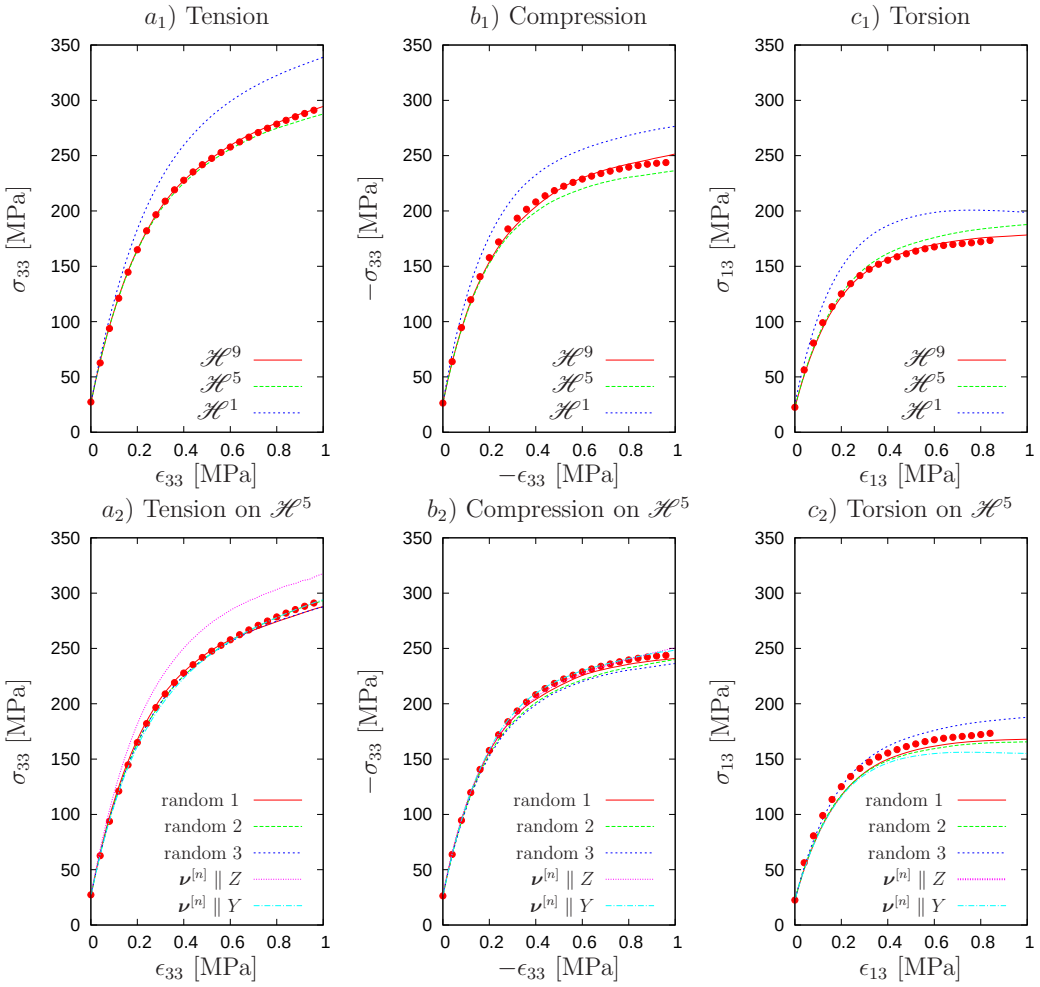

Fig. 6. Macroscopic stress-strain response of polycrystalline copper predicted by present model in tension (a), compression (b), and torsion (c). The experimental data of Tomé et al. (1984) are indicated by dots. $\mathscr{H}^1$ is the same as the Taylor model.

The first row of Fig. 6 compares the calculated stress-strain curves obtained from the present model for tensile (Fig. 6a$_1$), compressive (Fig. 6b$_1$), and torsional (Fig. 6c$_1$) deformation imposed on $\mathscr{H}^1$, $\mathscr{H}^5$, and $\mathscr{H}^9$ with the experimental data of Tomé et al. (1984). It is seen that both the true binary-tree based models, $\mathscr{H}^5$, and $\mathscr{H}^9$, predict similar macroscopic response. The Taylor model ($\mathscr{H}^1$) however predicts a significantly harder response than the true binary-tree based models.

The initial orientations of the interfacial normals $\{\boldsymbol{\nu}^{[n]}\colon n \in \mathscr{N}[r]\}$ between sub-aggregates were kept the same in calculating all the stress-strain curves of the first row of Fig. 6. These initial orientations were realized from a uniform distribution over the unit sphere. The second row of Fig. 6 considers the effect

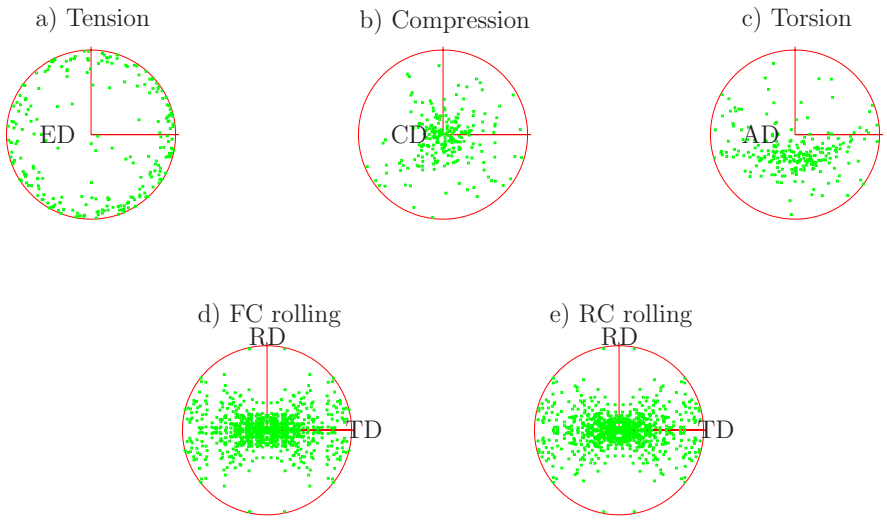

Fig. 7. Orientations of the normal vectors of the grain-boundaries between sibling grains in the binary-tree based model (interfaces between the leaves of the binary tree), after tension (a), compression (b), torsion (c), FC rolling (d), and RC rolling (e) deformation imposed on $\mathscr{H}^9$. ED is the extension direction, CD the compression direction, AD the axial direction, RD the rolling direction, and TD the transverse direction.

of varying the initial orientations. Curves labeled 'random 1', 'random 2', and 'random 3' correspond to different realizations of $\{\boldsymbol{\nu}^{[n]} : n \in \mathscr{N}[r]\}$ drawn from a uniform distribution over the unit sphere. Additionally, cases assuming that the interfaces for all $n \in \mathscr{N}[r]$ are oriented according to $\boldsymbol{\nu}^{[n]} \parallel Z$ and $\boldsymbol{\nu}^{[n]} \parallel Y$ are also considered. It is seen that all three statistically equivalent initial interfacial orientations considered produce comparable macroscopic stress-strain curves, with the greatest deviations occurring in full-constraints torsion. The tensile stress-strain curve corresponding to $\boldsymbol{\nu}^{[n]} \parallel Z$ in Fig. $6a_2$ deviates the most from the other curves plotted for tension in the same figure, whereas the response in compression shown in Fig. $6b_2$ is insensitive to the initial distribution of interfacial normals.

The orientation of the interfacial normals $\boldsymbol{\nu}^{[n]}$ between sub-aggregates evolves with deformation. Fig. 7 shows the calculated $\boldsymbol{\nu}^{[n]}$ between leaf nodes in the binary tree. Physically, these orientations correspond to the grain-boundary normal between two grains. It is clear that after tension the $\boldsymbol{\nu}^{[n]}$ cluster normal to the extension direction; after compression they cluster along the compression direction; and after torsion they cluster between the torsional axis and the torsional direction. These predictions agree with the experimental observations of Tomé et al. (1984).

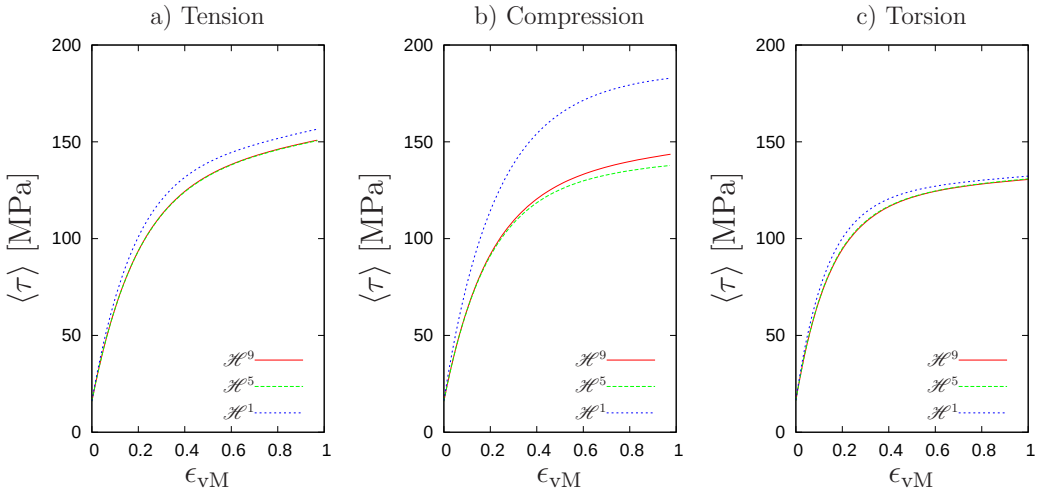

Fig. 8. Evolution with tensile and compressive deformation of the average critical resolved shear stress $\langle\tau\rangle$ defined in Eq. (64).

Table 2
$\langle N_{\text{act}}\rangle$ averaged over the entire deformation for different loading types imposed upon the node sets $\mathscr{H}^9$, $\mathscr{H}^5$, and $\mathscr{H}^1$.

	$\mathscr{H}^9$	$\mathscr{H}^5$	$\mathscr{H}^1$
Tension	2.87	2.86	2.91
Compression	2.87	2.86	2.85
Torsion	2.82	2.96	4.32
FC Rolling	2.84	2.96	4.33
RC Rolling	2.84	2.83	2.62

Fig. 8 plots the evolution of $\langle\tau\rangle$, the critical resolved shear stress averaged over all grains, defined as

$$\langle\tau\rangle = \sum_{k\in\mathscr{L}[r]} \frac{w^{[k]}}{w^{[r]}} \frac{1}{S} \sum_{s=1}^{S} \tau_s^{[k]}. \tag{64}$$

We may regard the evolution of $\langle\tau\rangle$ as the hardening of the average slip system in the average grain. It is seen in Fig. 8 that the average slip-system hardens more in the Taylor model than in the true binary-tree based models for all three loading conditions considered. However, the enhanced hardening in the Taylor simulations compared to that in the true binary-tree based simulations is much more pronounced in compression than in tension or torsion.

An important measure of deformation partitioning among grains is the average

number of active slip systems, $\langle N_{\rm act}\rangle$, defined as

$$\langle N_{\rm act}\rangle = \sum_{k\in\mathscr{L}[r]} \frac{w^{[k]}}{w^{[r]}} \sum_{s=1}^{S} \mathbf{1}_{[\dot\gamma_s^{[k]}>0]}. \tag{65}$$

$\langle N_{\rm act}\rangle$ may be regarded as the number of slip systems having non-zero slip-rate in the average grain. In calculations assuming a true binary-tree based model, $\langle N_{\rm act}\rangle$ remains approximately constant over the deformation history for all deformation modes considered: tension, compression, and torsion. Further, the average $\langle N_{\rm act}\rangle$ over the deformation history varies over a relatively narrow range of $2.82 \leq \langle N_{\rm act}\rangle \leq 2.96$.

Interestingly, the average $\langle N_{\rm act}\rangle$ assuming the Taylor model ($\mathscr{H}^1$ loading) of tension and compression, with constraints relaxed according to Eq. (62), is comparable to that of the true binary-tree based model in tension and compression. Full constraints simulation of torsion according to Eq. (63) using the Taylor model, however, results in a markedly larger value of $\langle N_{\rm act}\rangle$. The values of $\langle N_{\rm act}\rangle$ in the present model is smaller by about 1.0 than that obtained from the rate-independent model of I.

The above observations will now be interpreted in light of a viewpoint due to Tomé et al. (1984). This viewpoint maintains that the macroscopic stress-strain response is determined in part by how the macroscopically imposed deformation is partitioned amongst grains, and partly by how the deformation imposed upon a grain is accommodated by the activity of its slip systems. These distinct contributors to the macroscopic response are presently termed inter-granular, and intra-granular factors, respectively. Texturing of lattice orientations, and interactions arising from compatibility conditions between sub-aggregates represented by sibling nodes in the binary tree, constitute inter-granular factors in the present model. Latent hardening of slip systems as described in Sec. 2.2 is the key intra-granular factor in the present model. Since slip systems in a grain activate and harden in response to the deformation imposed on it, which in turn depends on the intergranular interactions, the inter- and intragranular factors are inseparable on the basis of macroscopic observations of the mechanical response alone. The various binary-tree based models studied here, $\mathscr{H}^1$ (Taylor), $\mathscr{H}^5$, and $\mathscr{H}^9$ allow us a means to impose different inter-granular interaction mechanisms, while keeping fixed the intra-granular factors. They therefore allow separate consideration of the two factors on the overall macroscopic response.

It is seen from Figs. $6a_1$, $6b_1$, and $6c_1$ that the Taylor $\mathscr{H}^1$ model predicts a significantly harder response than the true binary-tree based models under all types of loading: tension, compression, and torsion. From Fig. 8b, however, it is seen that substantially larger hardening of slip systems in $\mathscr{H}^1$ (Taylor) simulations compared to that in true binary-tree based ($\mathscr{H}^5$ or $\mathscr{H}^9$) simu-

lations occurs only in compression. In tension and in torsion, as seen from Figs. 8a, and 8c, the enhancement of $\langle\tau\rangle$ in Taylor $\mathscr{H}^1$ simulations compared to the true binary-tree based $\mathscr{H}^5$ or $\mathscr{H}^9$ simulations is less pronounced than in Fig. 8b. Together, these observations suggest that the inter-granular factor dominates in determining the macroscopic response under tension and torsion, and that the intra-granular factor dominates in determining the same under compression.

Inter-granular factor dominance in tension also explains the large difference between the calculated stress-strain response assuming $\boldsymbol{\nu}^{[n]} \parallel Z$ in Fig. 6a$_2$ and the other curves in the same figure: As seen in Fig. 7a the assumption $\boldsymbol{\nu}^{[n]} \parallel Z$ in Fig. 6a$_2$ contradicts the actual distribution of the interface normals in a polycrystal under tension, which follows $\boldsymbol{\nu}^{[n]} \perp Z$. However, by the same reasoning, the compression stress-strain curve in Fig. 6b$_2$ that assumes $\boldsymbol{\nu}^{[n]} \parallel Y$ must diverge significantly from the other curves in Fig. 6b$_2$. This divergence is absent owing to the relative unimportance of the inter-granular factor in compression, and the dominance of the intra-granular factor in compression, as noted above.

3.2 Texture evolution during plane-strain deformation

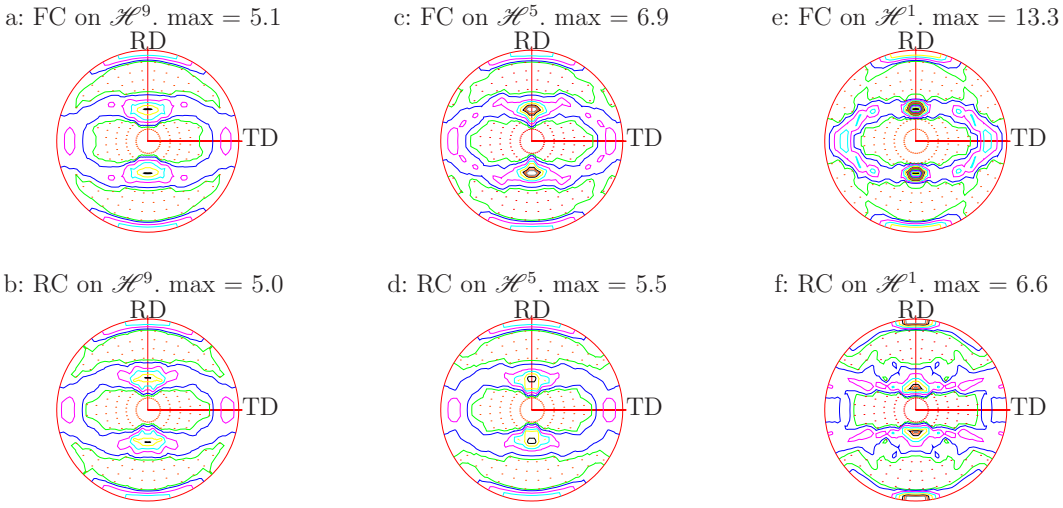

Fig. 9. Calculated {111} pole figures after a rolling reduction of 74% from $N_g = 256$ grain simulations using the present model. Four-fold symmetrization of the pole figures and the choice of the level lines $(0.5, 1, 2, 3, \ldots, 13)$ are done to aid comparison with the experimental pole figure of Hirsch and Lucke (1988a).

We now turn to the response of the binary-tree based polycrystal to im-

posed plane-strain deformation. Full constraints (FC) deformation refers to the boundary condition wherein the velocity gradient

$$[\boldsymbol{L}^{[r]}]_{XYZ} = \begin{pmatrix} 1 & 0 & 0 \\ 0 & 0 & 0 \\ 0 & 0 & -1 \end{pmatrix}, \tag{66}$$

is imposed upon the root node r of the binary tree. Relaxed constraints (RC) refers to the boundary condition

$$[\boldsymbol{L}^{[r]}]_{XYZ} = \begin{pmatrix} 1 & \cdot & \cdot \\ 0 & 0 & 0 \\ 0 & 0 & -1 \end{pmatrix}, \tag{67}$$

wherein the components $L_{12}^{[r]}$ and $L_{13}^{[r]}$ are left unspecified, but the corresponding stress components σ_{12}, and σ_{13} are set equal to zero (Honneff and Mecking, 1978). We note from Eq. (66) that the rolling, transverse, and normal directions are parallel to the X, Y, and Z axes, respectively.

Fig. 9 shows the textures calculated after 74% rolling reduction. As seen from Fig. 9 (a-d), all four true binary-tree based models subjected to either FC or RC loading result in a similar end texture with a peak intensity that is comparable to the experimentally observed (Hirsch and Lucke, 1988a) final peak intensity of 6, and also to the predictions of the rate-dependent simulations ($n = 20$) described in I. Similarity of the end textures of the true binary-tree based models was seen in the rate-dependent model of I also, suggesting that the observed insensitivity of the texture predictions to the imposed boundary conditions is controlled primarily by the inter-granular influence, particularly compatibility constraints between grains in the present simulations. The FC Taylor simulation with loading imposed on $\mathscr{H}^1$ over-predicts the texturing rate by far as seen in Fig. 9e. This is in agreement with the observations of earlier studies (Leffers, 1975, Hirsch and Lucke, 1988b, Lee and Duggan, 1993). The RC Taylor simulation with loading imposed on $\mathscr{H}^1$ however, predicts a peak textural intensity that is comparable to the experimental value, as seen in Fig. 9f. This agrees with the observation of Honneff and Mecking (1978).

We will investigate the success of the RC Taylor mode of deformation shown in Fig. 9f further. To this end, Fig. 10 compares the axes of instantaneous lattice rotation in the binary-tree based model with FC imposed upon $\mathscr{H}^9$ (first row) with RC imposed upon the grains of $\mathscr{H}^1$ (second row) at stages early in the simulated deformation (first column), and mid-way through the simulated deformation (second column). Although there are differences in the intensities of the lattice rotation vectors in the four cases, it is clear that

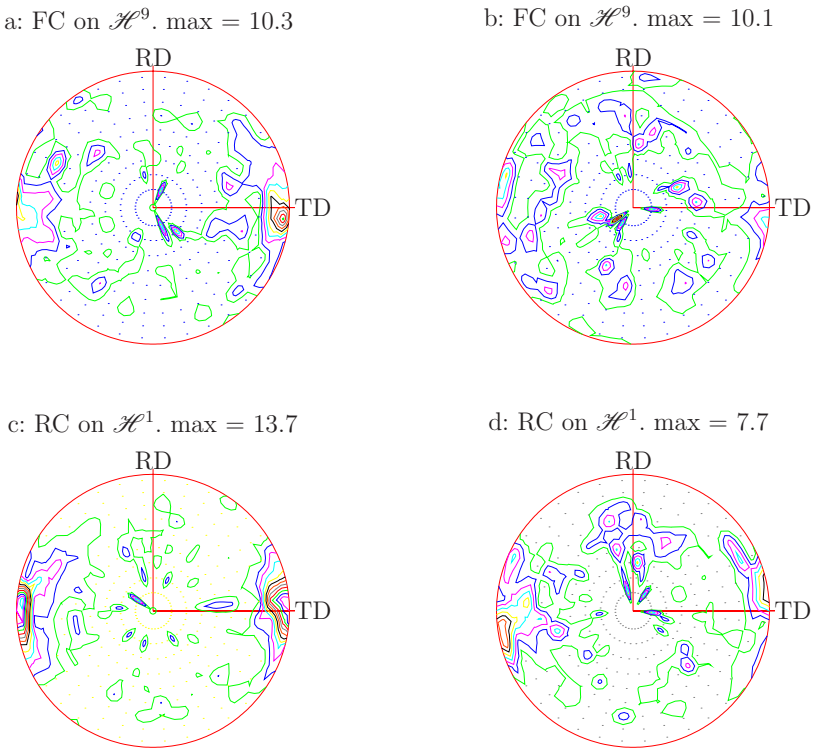

Fig. 10. Calculated distributions of the lattice spin vector during rolling assuming imposed FC on $\mathscr{H}^9$ after 6% (a) and 38% (b) rolling reductions, and assuming imposed RC on $\mathscr{H}^1$ after 6% (c) and 38% (d) rolling reductions. The contours correspond to $1, 2, \ldots$.

the lattice rotation vector is predominantly concentrated along the transverse direction in both cases. This suggests that the paths by which the grains rotate to the end orientations shown in Figs. 9a, and 9f are similar, as are the final textures themselves.

The evolution of the sub-structure in the case of the true binary-tree based models and in the case of the RC Taylor model is also similar. This is seen by studying the average number of active slip systems $\langle N_{\text{act}} \rangle$. $\langle N_{\text{act}} \rangle$ does not vary much over the history of deformation and the values of $\langle N_{\text{act}} \rangle$ averaged over the entire deformation are given in Table 2. It is noteworthy that $\langle N_{\text{act}} \rangle$ in the true binary-tree based models is only slightly larger than that in the Taylor RC model ($\mathscr{H}^1$). However, fewer slip systems get activated in the present rate-independent study than in the rate-dependent study of I as revealed by comparison with Fig. 5 of I. FC Taylor simulation ($\mathscr{H}^1$; Fig. 9e) results in the activation of more slip systems than that in any of the other models. This appears to underlie the prediction of excessive texturing in the FC Taylor

simulation.

Since the relaxation of the $L_{12}^{[r]}$ and $L_{13}^{[r]}$ components in Eq. (66) brings qualitative agreement between the peak texture intensities, distribution of lattice rotation vectors and $\langle N_{\rm act}\rangle$ of the true binary-tree based models and the RC $\mathscr{H}^1$ Taylor model, we now inquire if the stress-state within grains during rolling deformation in the true binary-tree based models conforms approximately to the Taylor RC condition of $\sigma_{12}^{[k]} = \sigma_{13}^{[k]} = 0$, for $k \in \mathscr{L}[r]$. To this end, we define a non-dimensional rolling-plane shear traction parameter, $\psi_{12,13}^{[h]}$ as

$$\psi_{12,13}^{[h]} = \frac{\sum_{k\in\mathscr{H}^{[h]}}(w^{[k]}/w^{[r]})\sqrt{\left(\sigma_{12}^{[k]}\right)^2 + \left(\sigma_{13}^{[k]}\right)^2}}{\sqrt{(3/2)\boldsymbol{\sigma}^{[r]} : \boldsymbol{\sigma}^{[r]}}}. \tag{68}$$

Note that the denominator of the right-side of Eq. (68) is the von Mises stress in the polycrystal. In the case of RC Taylor loading applied to grains, $\psi_{12,13}^{[1]} = 0$. The deviation from zero of $\psi_{12,13}^{[1]}$ for the true binary-tree based models indicates the extent of violation of the RC condition therein.

Fig. 11 shows the rolling-plane shear traction parameter in the binary-tree based model computed at various heights h in the binary tree. It is evident that the rolling-plane shear traction factors at the level of the grains ($h = 1$) are comparable regardless of the constraints imposed at the root node. Thus, $\psi_{12,13}^{[h]} \approx 0.2$ for $h = 1$, except when RC loading is imposed upon $\mathscr{H}^1$, in which case, $\psi_{12,13}^{[1]} = 0$ by definition. Further, $\psi_{12,13}^{[h]}$ diminishes by the averaging out of shear traction components about a zero mean with increasing h. Thus the assumption of Honneff and Mecking (1978), viz., $\sigma_{12}^{[k]} = \sigma_{13}^{[k]} = 0$, for $k \in \mathscr{L}[r]$, is not supported by the true binary-tree based models. In other words, the assumption of null shear tractions in the grains of the RC model of Honneff and Mecking (1978) overestimates the relaxation of $\sigma_{12}^{[k]}$ and $\sigma_{13}^{[k]}$, for $k \in \mathscr{L}[r]$, but in such a manner that the number of slip systems activated in the average grain is still reasonably estimated, leading to the comparable texture evolution in the true binary-tree based models and the Taylor RC model.

It is noted that a quantitative comparison of the texture predictions with experimental textures, or texture predictions by other models has not been undertaken here, and remains to be performed. Such a comparison must begin with the measured initial texture, and may either quantify the differences between two compared textures by an integral over Euler space of the square of the difference between the two texture intensities as done by Van Houtte et al. (2004), or by comparing the evolution of the intensity along skeleton lines of the two textures as done by Engler et al. (2005). Lacking such a quantitative comparison, it is not possible to judge the quality of the textures predicted by the present model relative to other models.

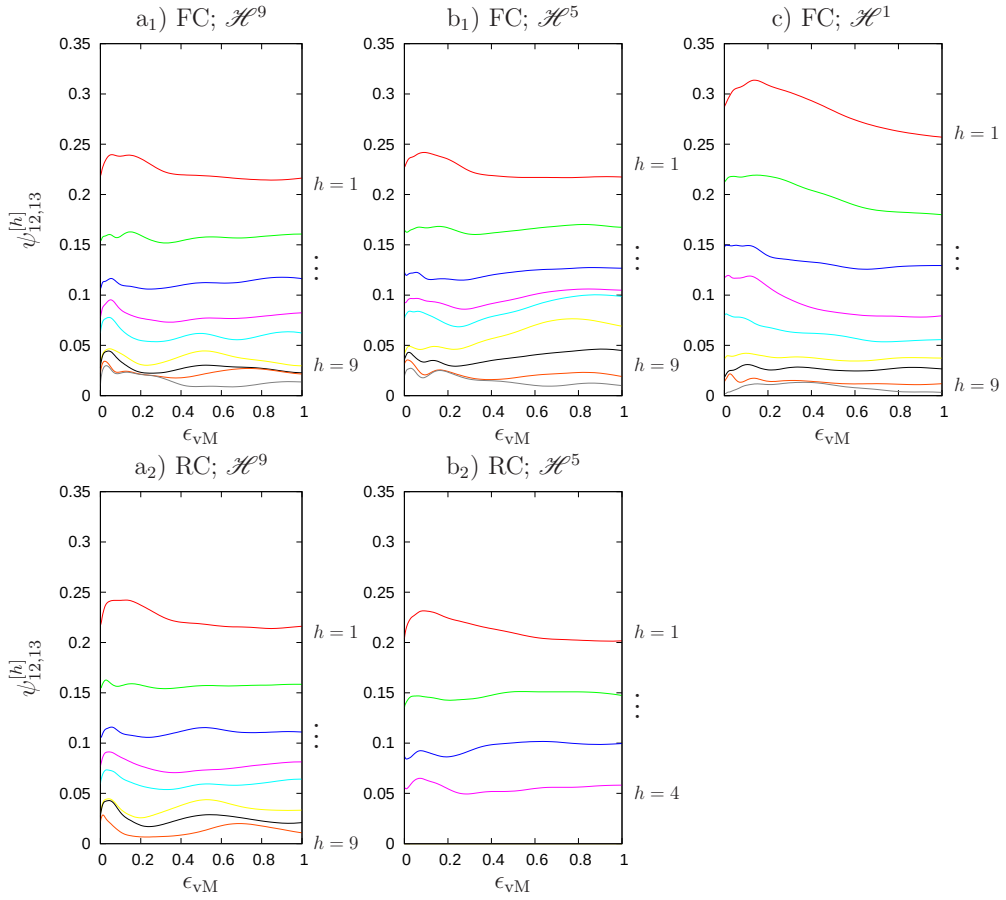

Fig. 11. Evolution of the rolling-plane shear traction factor $\psi^{[h]}_{12,13}$ with deformation at different heights $h = 1, 2, 3, \ldots$ of the binary tree assuming full constraints imposed upon $\mathscr{H}^9$ (a_1), $\mathscr{H}^5$ (b_1) and $\mathscr{H}^1$ (c), and assuming relaxed constraints imposed upon $\mathscr{H}^9$ (a_2) and $\mathscr{H}^5$ (b_2).

3.3 Computational effort

The rate-independent Taylor model is considerably faster than the rate-dependent Taylor model of I (with reciprocal rate-sensitivity 20) by a factor of ~ 15. Within the class of rate-independent models, the computation times are comparable: Tensile simulation of the 256 grain binary-tree based model shown in Fig. 5 to a von Mises strain of about 1.0 requires $1.2\times$ for loading imposed on $\mathscr{H}^5$ and $1.9\times$ for loading imposed on $\mathscr{H}^9$ relative to the computer time required to simulate the same deformation of the same polycrystal using the Taylor $\mathscr{H}^1$ model. On an ordinary PC with a single 2 GHz processor, wall-clock computation time for the Taylor $\mathscr{H}^1$ model was on average, 0.00216 seconds per step per grain. This increased to 0.00416 seconds per step per grain in the $\mathscr{H}^9$ simulation. Computational effort scaling for the binary-tree

based model relative to the Taylor model for other loading paths are similar.

4 Conclusions

(1) A rate-independent version of the binary-tree based model is proposed. It is shown that an extension of Taylor's principle that determines the activation of slip systems applies to the binary-tree based polycrystal.
(2) The rate-independent binary-tree based model is employed to simulate monotonic tension, compression, torsion and plane strain deformation of a copper polycrystal and succeeds in fitting experimentally observed macroscopic responses. The computation time of the binary-tree based model is of the same order as that of the classical Taylor model.
(3) Continuity of traction and velocity fields between sub-aggregates represented by sibling nodes in the binary tree has a significant influence on the predictions of the model, as evidenced by the markedly different predictions of the stress-strain response in the true binary-tree based models and Taylor type models.
(4) The sensitivity of the model to assumptions about the interfacial orientation distribution, depends on whether microstructural or sub-structural influences determine the macroscopic response, which in turn, depends upon the loading path.
(5) The binary-tree based model was used to analyze the success of the Taylor RC model of Honneff and Mecking (1978) in predicting the correct peak texture intensity after rolling. It is found that the granular stress-state assumed by Honneff and Mecking (1978) underestimates the rolling plane shear tractions by assuming them to be zero. Nevertheless, this assumption causes a relatively small underestimation of the number of slip systems activated in RC rolling simulations compared to the binary-tree based model and results in comparable end textures predicted by the Taylor RC model and the true binary-tree based models.

Acknowledgment: The author gratefully acknowledges using the software `POLE` developed by Dr. C. N. Tomé of Los Alamos National Laboratory to generate the pole figures shown here. The author also thanks Mr. M. Arul Kumar and the anonymous referees of this manuscript for suggestions that helped improve it. Funding for this work was provided by the Indira Gandhi Center for Atomic Research, Kalpakkam.

References

Aernoudt, E., Van Houtte, P., Leffers, T., 1993. Plastic Deformation and Fracture of Materials. Vol. 6 of Materials Science and Technology: A Comprehensive Treatment. VCH, Ch. Deformation and textures of metals at large strains, pp. 89–136.

Amirkhizi, A. V., Nemat-Nasser, S., 2007. A framework for numerical integration of crystal elasto-plastic constitutive equations compatible with explicit finite element codes. Int. J. Plast. 23 (10-11), 1918–1937.

Arsenlis, A., Barton, N. R., Becker, R., Rudd, R. E., 2006. Generalized in situ adaptive tabulation for constitutive model evaluation in plasticity. Comput. Methods Appl. Mech. Eng. 196, 1–13.

Asaro, R., Lubarda, V., 2006. Mechanics of Solids and Materials. Cambridge University Press.

Asaro, R. J., Needleman, A., 1985. Overview 42. Texture development and strain-hardening in rate dependent polycrystals. Acta metall. 33 (6), 923–953.

Ashby, M. F., 1970. The deformation of plastically non-homogeneous materials. Phil. Mag. 21 (170), 399.

Barbe, F., Decker, L., Jeulin, D., Cailletaud, G., 2001. Intergranular and intragranular behavior of polycrystalline aggregates. part 1: F.E. model. Int. J. Plast. 17 (4), 513–536.

Barton, N. R., Knap, J., Arsenlis, A., Becker, R., Hornung, R. D., Jefferson, D. R., 2008. Embedded polycrystal plasticity and adaptive sampling. Int. J. Plast. 24 (2), 242–266.

Beaudoin, A. J., Dawson, P. R., Mathur, K. K., Kocks, U. F., 1995. A hybrid finite element formulation for polycrystal plasticity with consideration of macrostructural and microstructural linking. Int. J. Plast. 11 (5), 501–521.

Beaudoin, A. J., Mathur, K. K., Dawson, P. R., Johnson, G. C., 1993. Three-dimensional deformation process simulation with explicit use of polycrystal plasticity models. Int. J. Plast. 9 (7), 833–860.

Bishop, J. F. W., Hill, R., 1951. A theory of the plastic distortion of a polycrystalline aggregate under combined stresses. Phil. Mag. 42 (327), 414–427.

Chin, G. Y., Mammel, W. L., 1969. Generalization and equivalence of the minimum work (Taylor) and Maximum work (Bishop-Hill) Principles of Crystal Plasticity. Trans. AIME 245, 1211.

Cormen, T. H., Leiserson, C. E., Rivest, R. L., 1990. Introduction to Algorithms. MIT press, Cambridge.

Dantzig, G. B., 1963. Linear programming and extensions. Princeton University Press, Princeton, New Jersey.

Engler, O., Crumbach, M., Li, S., 2005. Alloy-dependent rolling texture simulation of aluminium alloys with a grain-interaction model. Acta mater. 53 (8), 2241–2257.

Fleck, N. A., Ashby, M. F., Hutchinson, J. W., 2003. The role of geometrically necessary dislocations in giving material strengthening. Scripta mater. 48,

179–183.
Franciosi, P., Zaoui, A., 1982. Multislip in FCC crystals: A theoretical approach compared with experimental data. Acta metall. 30, 1627–1637.
Fuh, S., Havner, K. S., 1989. A theory of minimum plastic spin in crystal mechanics. Proc. R. Soc. Lond. A422, 193–239.
Ganapathysubramanian, S., Zabaras, N., 2005. Modeling the thermoelastic-viscoplastic response of polycrystals using a continuum representation over the orientation space. Int. J. Plast. 21 (1), 119–144.
Garmestani, H., Lin, S., Adams, B. L., Ahzi, S., 2001. Statistical continuum theory for large plastic deformation of polycrystalline materials. J. Mech. Phys. Solids 49 (3), 589–607.
Gil Sevillano, J., Houtte, P. V., Aernoudt, E., 1980. Geometical models for polycrystal deformation and texture prediction. Prog. Mater. Sci. 25 (2-4), 272–341.
Guan, Y., Pourboghrat, F., Barlat, F., 2006. Finite element modeling of tube hydroforming of polycrystalline aluminum alloy extrusions. Int. J. Plast. 22 (12), 2366–2393.
Gurtin, M. E., 1981. An introduction to continuum mechanics. Academic Press, New York.
Haddadi, H., Bouvier, S., Banu, M., Maier, C., Teodosiu, C., 2006. Towards an accurate description of the anisotropic behaviour of sheet metals under large plastic deformations: Modelling, numerical analysis and identification. Int. J. Plast. 22 (12), 2226–2271.
Havner, K. S., 1971. A discrete model for the prediction of subsequent yield surfaces in polycrystalline plasticity. Int. J. Solids Struct. 7, 719–730.
Havner, K. S., 1992. Finite Plastic Deformation of Crystalline Solids. Cambridge University Press.
Héripré, E., Dexet, M., Crépin, J., L. Gélébart, A. R., Bornert, M., Caldemaison, D., 2007. Coupling between experimental measurements and polycrystal finite element calculations for micromechanical study of metallic materials. Int. J. Plast. 23 (9), 1512–1539.
Hill, R., 1961. Discontinuity relations in mechanics of solids. In: Sneddon, I. N., Hill, R. (Eds.), Progress in Solid Mechanics. Vol. 2. Interscience Publishers, New York, Ch. 6, pp. 247–278.
Hill, R., 1965. Continuum micro-mechanics of elastoplastic polycrystals. J. Mech. Phys. Solids 13, 89–101.
Hill, R., 1966. Generalized constitutive relations for incremental deformation of metal crystals by multislip. J. Mech. Phys. Solids 14 (2), 95–102.
Hill, R., 1967. The essential structure of constitutive laws for metal composites and polycrystals. J, Mech. Phys. Solids 15, 79–95.
Hirsch, J., Lucke, K., 1988a. Mechanism of deformation and development of rolling textures in polycrystalline FCC metals: I Description of rolling texture in homogeneous CuZn alloys. Acta metall. 36 (11), 2863–2882.
Hirsch, J., Lucke, K., 1988b. Mechanism of deformation and development of rolling textures in polycrystalline FCC metals: II Simulation and interpre-

tation of experiments on the basis of Taylor-type theories. Acta metall. 36 (11), 2883–2904.

Honneff, H., Mecking, H., 1978. A method for the determination of the active slip systems and orientation changes during single crystal deformation. In: Proc. 5th Int. Conf. on the Textures of Materials. Vol. 1. Springer-Verlag, pp. 265–275.

Hosford, W. F., 1993. The mechanics of crystals and textured polycrystals. Oxford University Press, New York.

Hutchinson, J. W., 1976. Bounds and self-consistent estimates for creep of polycrystalline materials. Proc. R. Soc. Lond. A. 348 (1652), 101–127.

Kalidindi, S. R., Bronkhorst, C. A., Anand, L., 1992. Crystallographic texture evolution in bulk deformation processing of FCC metals. J. Mech. Phys. Solids, 537–569.

Kalidindi, S. R., Duvvuru, H. K., 2005. Spectral methods for capturing crystallographic texture evolution during large plastic strains in metals. Acta mater. 53 (13), 3613–3623.

Kalidindi, S. R., Duvvuru, H. K., Knezevic, M., 2006. Spectral calibration of crystal plasticity models. Acta Mater. 54 (7), 1795–1804.

Kim, J. H., Lee, M.-G., Barlat, F., Wagoner, R. H., Chung, K., 2008. An elasto-plastic constitutive model with plastic strain rate potentials for anisotropic cubic metals. Int. J. Plast. 24 (12), 2298–2334.

Knezevic, M., Kalidindi, S. R., Fullwood, D., 2008. Computationally efficient database and spectral interpolation for fully plastic Taylor-type crystal plasticity calculations of face-centered cubic polycrystals. Int. J. Plast. 24, 1264–1276.

Kocks, U. F., Tomé, C. N., Wenk, H. R., 1998. Texture and Anisotropy. Cambridge University Press, Cambridge, U.K.

Kröner, E., 1961. Zur plastischen verformung des vielkristalls. Acta metall. 9, 155–161.

Lebensohn, R., 1999. Modeling the role of local correlations in polycrystal plasticity using viscoplastic self-consistent schemes. Modeling Simul. Mater. Sci. Eng. 7, 739–746.

Lebensohn, R., Ühlenhut, H., Hartig, C., Mecking, H., 1998a. Plastic flow of γ-TiAl-based polysynthetically twinned crystals: micromechanical modeling, and experimental validation. Acta mater. 46 (13), 4701–4709.

Lebensohn, R. A., Turner, P. A., Signorelli, J. W., Canova, G. R., Tomé, C. N., 1998b. Calculation of intergranual stresses based on a large strain visoplastic self-consistent polycrystal model. Modelling Simul. Mater. Sci. Eng. 6, 447–465.

Lebensohn, R. E., Tomé, C. N., 1993. A self-consistent anisotropic approach for the simulation of plastic deformation and texture development of polycrystals: application to zirconium alloys. Acta metall. mater. 41 (9), 2611–2624.

Lee, B. J., Ahzi, S., Parks, D. M., 2002. Bicrystal-based modeling of plasticity in FCC metals. J. Eng. Mater. Tech. 124 (1), 27.

Lee, C. S., Duggan, B. J., 1993. Studies on the sharpness of simulated defor-

mation textures. Scripta metall. mater. 28 (1), 121–126.
Lee, E. H., 1969. Elastic-plastic deformation at finite strains. J. Appl. Mech. 36, 1–6.
Leffers, T., 1975. On the misfit between the grains in a deformed sachs polycrystal and its relation to the inhomogeneous deformation of real polycrystals. Scripta metall. 9, 261–264.
Leffers, T., 1978. The shortcomings of the Taylor model in the description of the plastic deformation of real polycrystals. In: Proc. 5th Int. Conf. on the Textures of Materials. Vol. 1. Springer-Verlag, pp. 277–287.
Leffers, T., Christoffersen, H., 1997. The importance of grain-to-grain interaction during rolling deformation of copper. Mater. Sci. Eng. A234–236, 676–679.
Logé, R. E., Chastel, Y. B., 2006. Coupling the thermal and mechanical fields to metallurgical evolutions within a finite element description of a forming process. Comput. Method. Appl. Mech. 195 (48-49), 6843–6857.
Mahesh, S., 2006. Deformation banding and shear banding in single crystals. Acta mater. 54 (17), 4565–4574.
Mahesh, S., 2009. A hierarchical model for rate-dependent polycrystals. Int. J. Plast. 25 (5), 752–767.
Manonukul, A., Dunne, F. P. E., 2004. High- and low-cycle fatigue crack initiation using polycrystal plasticity. Proc. R. Soc. A 460 (2047), 1881–1903.
Mathur, K. K., Dawson, P. R., 1989. On modeling the development of crystallographic texture in bulk forming processes. Int. J. Plast. 5 (1), 67–94.
Mika, D. P., Dawson, P. R., 1998. Effects of grain interaction on deformation in polycrystals. Mater. Sci. Eng. A 257 (1), 62–76.
Molinari, A., Canova, G. R., Ahzi, S., 1987. A self consistent approach of the large deformation polycrystal viscoplasticity. Acta metall. 35, 2983–2994.
Pan, J., Rice, J. R., 1983. Rate-sensitivity of plastic flow and implications for yield-surface vertices. Int. J. Solids Struct. 19 (11), 973–987.
Pierce, D., Asaro, R. J., Needleman, A., 1982. An analysis of nonuniform and localized deformation in ductile single crystals. Acta mater. 30, 1087–1119.
Pierce, D., Asaro, R. J., Needleman, A., 1983. Material rate dependence and localized deformation in crystalline solids. Acta metall. 31 (12), 1951–1976.
Proust, G., Tomé, C. N., Kaschner, G. C., 2007. Modeling texture, twinning and hardening evolution during deformation of hexagonal materials. Acta mater. 55, 2137–2148.
Rice, J. R., 1971. Inelastic constitutive relations for solids: An internal-variable theory and its application to metal plasticity. J. Mech. Phys. Solids 19 (6), 433–455.
Rockafellar, R. T., 1970. Convex analysis. Princeton University Press, Princeton, New Jersey.
Sachs, G., 1928. Zur Ableitung einer Fliessbedingung. Z. Ver. Dtsch. Ing. 72, 734–736.
Saran, M., 1991. Comparison of elastic-plastic and rigid-plastic implicit FEM simulations in sheet forming applications. J. Mater. Proc. Tech. 27 (1–3),

279–300.
Taylor, G. I., 1938. Plastic strain in metals. J. Inst. Met. 62, 307.
Tomé, C., Canova, G. R., Kocks, U. F., Christodoulou, N., Jonas, J. J., 1984. The relation between macroscopic and microscopic strain hardening in F.C.C polycrystals. Acta metall. 32 (10), 1637–1653.
Van Houtte, P., Aernoudt, E., 1975a. Solution of the generalized Taylor theory of plastic flow. I and II. Z. Metallkde. 66, 202–209.
Van Houtte, P., Aernoudt, E., 1975b. Solution of the generalized Taylor theory of plastic flow. III Applications. Z. Metallkde. 66, 303–306.
Van Houtte, P., Delannay, L., Kalidindi, S. R., 2002. Comparison of two grain interaction models for polycrystal plasticity and deformation texture prediction. Int. J. Plast. 18 (3), 359–377.
Van Houtte, P., Delannay, L., Samajdar, I., 1999. Quantitative predictions of the cold-rolling texture in low-carbon steel by means of the LAMEL model. Texture microstruct 31 (3), 104–119.
Van Houtte, P., Kanjarla, A. K., Van Bael, A., Seefeldt, M., Delannay, L., 2006. Multiscale modelling of the plastic anisotropy and deformation texture of polycrystalline materials. Eur J Mech. A 25 (4), 634–648.
Van Houtte, P., Li, S., Engler, O., 2004. Modelling deformation texture of aluminium alloys using grain interaction models. Aluminium 80, 702–706.
Van Houtte, P., Li, S., Seefeldt, M., Delannay, L., 2005. Deformation texture prediction: from the Taylor model to the advanced lamel model. Int. J. Plast. 21 (3), 589–624.
Van Houtte, P., Yerra, S. K., Van Bael, A., 2009. The facet method: A hierarchical multilevel modelling scheme for anisotropic convex plastic potentials. Int. J. Plast. 25 (2), 332–360.
Wang, Z. Q., Beyerlein, I. J., LeSar, R., 2008. Plastic anisotropy in fcc single crystals in high rate deformation. Int. J. Plast. 25 (1), 26–48.
Zhang, F., Bower, A. F., Mishra, R. K., Boyle, K. P., 2008. Numerical simulations of necking during tensile deformation of aluminum single crystals. Int. J. Plast. 25 (1), 49–69.